



MONTCLAIR STATE
UNIVERSITY

Montclair State University
**Montclair State University Digital
Commons**

Theses, Dissertations and Culminating Projects

5-2022

New Black Carbon Isotopes from the Eastern Tethys and Earth System Modeling During the PETM

Maurizia De Palma
Montclair State University

Follow this and additional works at: <https://digitalcommons.montclair.edu/etd>



Part of the [Earth Sciences Commons](#), and the [Environmental Sciences Commons](#)

Recommended Citation

De Palma, Maurizia, "New Black Carbon Isotopes from the Eastern Tethys and Earth System Modeling During the PETM" (2022). *Theses, Dissertations and Culminating Projects*. 1013.
<https://digitalcommons.montclair.edu/etd/1013>

This Thesis is brought to you for free and open access by Montclair State University Digital Commons. It has been accepted for inclusion in Theses, Dissertations and Culminating Projects by an authorized administrator of Montclair State University Digital Commons. For more information, please contact digitalcommons@montclair.edu.

Abstract

The Paleocene-Eocene Thermal Maximum (PETM; *ca.* 56Ma) is a time when global temperatures greatly increased due to rapid carbon emissions. The event is marked by a negative carbon isotope excursion (CIE) that is observed in both marine and terrestrial records. However, the amount, rate, and source of the emitted carbon remains highly debated. This study investigates the response of the eastern Tethys, an understudied subtropical shallow marine environment, and assesses the climatic impacts during the PETM. An Earth system model of intermediate complexity (cGENIE) ran six “double-inversion” experiments with $\delta^{11}\text{B}$ and $\delta^{13}\text{C}_{\text{carb}}$ forced onto the surface ocean to assess the impacts of ocean acidification and determine the origin of the released carbon. Additionally, the eastern Tethys terrestrial paleoenvironment was reconstructed through black carbon (BC) isotopes, a paleo-fire archive, to determine how vegetation and precipitation responded during the PETM. The model shows that the eastern Tethys resists ocean acidification the longest by maintaining a comparatively higher pH than the global ocean. The diagnosed carbon flux reveals two distinct carbon emission pulses with different $\delta^{13}\text{C}$ signatures, suggesting that the North Atlantic Igneous Province (NAIP) could be the trigger mechanism for the PETM that then creates feedbacks into a second, more depleted carbon emission pulse. The $\delta^{13}\text{C}_{\text{BC}}$ values agree with bulk carbonates and *n*-alkane isotopes collected from the eastern Tethys, suggesting changes in regional precipitation shifted the vegetation type. Overall, understanding the Earth system responses in the eastern Tethys can infer carbon cycle history and evaluate the global and regional responses to the PETM.

Keywords: Paleoenvironment, Paleocene-Eocene Thermal Maximum (PETM), Kuzigongsu section, carbon isotopes, cGENIE, ocean acidification, black carbon

MONTCLAIR STATE UNIVERSITY

NEW BLACK CARBON ISOTOPES FROM THE EASTERN TETHYS AND EARTH
SYSTEM MODELING DURING THE PETM

by

Maurizia De Palma

A Master's Thesis Submitted to the Faculty of

Montclair State University

In Partial Fulfillment of the Requirements

For the Degree of

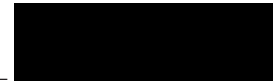
Master of Science

May 2022

College of Science and Mathematics

Department of Earth and Environmental Studies

Thesis Committee:

_____ 

Dr. Ying Cui

Thesis Sponsor

_____ 

Dr. Sandra Passchier

Committee Member

_____ 

Dr. Clement Alo

Committee Member

NEW BLACK CARBON ISOTOPES FROM THE EASTERN TETHYS AND
EARTH SYSTEM MODELING DURING THE PETM

A THESIS

Submitted in partial fulfillment of the requirements

For the degree of Master of Science

by

MAURIZIA DE PALMA

Montclair State University

Montclair, NJ

2022

Copyright © 2022 by *Maurizia De Palma*. All rights reserved

Acknowledgements

Starting my graduate studies during the COVID-19 pandemic was not easy, but I would like to thank all those that supported and guided me along the way. I would like to extend the utmost gratitude to my advisor, Dr. Ying Cui, for her patience, availability, and commitment with my thesis. This work introduced me to isotope geochemistry and challenged my abilities, but her mentoring developed this project to its full potential. Additionally, I want to thank my committee members: Dr. Sandra Passchier and Dr. Clement Alo. I thank you for taking interest in my project and for your flexibility. Your wisdom and helpful comments throughout this project furthered my understanding of the subject.

This work would not be possible without Dr. Xiaona Li, who assisted and guided me with the black carbon laboratory work and data analyzation. Also, special thanks to Dr. Andy Ridgwell for allowing us to use the sterling cluster to run our model experiments and answer our questions about the model's experimental methods. I would like to extend deep gratitude and appreciation to my paleoclimate lab members who graciously helped me with the lab work, stimulated interesting discussions, and loaned their support.

I would additionally like to extend my gratitude towards my friends and family who supported and encouraged me to continue throughout this journey. Finally, I would like to acknowledge the National Science Foundation Grant #2002370 for funding this research.

Table of Contents	
Abstract	1
Acknowledgements	5
Table of Contents	6
Table of Figures	7
List of Tables	9
Chapter 1: Multiple CO₂ emission pulses supported by new geochemical data in the eastern Tethys during the PETM	10
Abstract	10
1. Introduction	11
2. Methods	14
3. Results	18
<i>3.1 Cumulative carbon emission, emission rate, atmospheric pCO₂, and time-varying δ¹³C values</i>	18
<i>3.2 Warming and acidification of the global ocean</i>	23
<i>3.3 Organic carbon burial and the PETM recovery</i>	31
4. Discussion	35
<i>4.1 Determining the ¹³C-depleted source</i>	36
<i>4.2 Ocean acidification</i>	37
<i>4.3 Temperature and its effects</i>	38
<i>4.4 Organic carbon burial and the PETM recovery</i>	39
5. Conclusion	40
Chapter 2: New black carbon isotopes from the eastern Tethys during the PETM to investigate wildfire history	41
Abstract	41
1. Introduction	42
2. Geologic Background	44
3. Methods	45
4. Results	50
5. Discussion	56
6. Conclusion	60
Supplemental Figures	61
References	65

Table of Figures

Figure 1: The two CIE profiles.....	12
Figure 2: Carbon emission rate.....	19
Figure 3: Cumulative carbon flux.....	20
Figure 4: Atmospheric carbon dioxide.....	21
Figure 5: The $\delta^{13}\text{C}$ flux.....	22
Figure 6: Surface temperature differences.....	24
Figure 7: Surface ocean $\delta^{13}\text{C}_{\text{DIC}}$	25
Figure 8: The $\delta^{13}\text{C}_{\text{carb}}$ and $\delta^{11}\text{B}$ forcings against the model pH output.....	26
Figure 9: Surface ocean pH differences.....	27
Figure 10: Benthic Ω_{C} differences.....	28
Figure 11: Surface Ω_{C} differences.....	29
Figure 12: Surface dissolved O_2	30
Figure 13: Average benthic dissolved O_2	31
Figure 14: The organic carbon burial rate.....	33
Figure 15: The cumulative buried carbon.....	34
Figure 16: The average $\delta^{13}\text{C}$ for the buried organic carbon.....	35
Figure 17: Paleogeography during the PETM.....	45
Figure 18: Black carbon extraction procedure.....	49
Figure 19: $\delta^{13}\text{C}$ of black carbon against bulk carbonates.....	51
Figure 20: Frequency distribution of $\delta^{13}\text{C}_{\text{BC}}$	52
Figure 21: Average $\delta^{13}\text{C}_{\text{BC}}$ before and during the PETM.....	53
Figure 22: Terrestrial reconstruction proxies.....	

Figure 23: SEM image 1 of black carbon 55

Figure 24: SEM image 2 of black carbon 56

List of Tables

Table 1: cGENIE experimental descriptions	17
Table 2: Carbon emission pulses summaries	23
Table 3: Organic carbon burial experiments summary.....	35
Table 4: Black carbon samples	46

Chapter 1: Multiple CO₂ emission pulses supported by new geochemical data in the eastern Tethys during the PETM

Abstract

The Paleocene-Eocene Thermal Maximum (PETM; ~56 Ma) is a time when rapid carbon emissions caused perturbations to the global carbon cycle and global warming. However, there is much debate on the amount, rate, and source of carbon emitted during this time. While there are many studies that focused on ocean acidification in deep sea sites, there are limited studies on the climatic responses of the PETM in low latitude and shallow marine environments. The Earth system model cGENIE is utilized to create double-inversion experiments with $\delta^{13}\text{C}_{\text{carb}}$ and boron-based pH proxy data collected from the eastern Tethys and forced onto the surface ocean. The results show two distinct carbon emission pulses with different $\delta^{13}\text{C}$ signatures, suggesting the North Atlantic Igneous Province could have initiated the warming and carbon cycle feedbacks led to a second, more ^{13}C -depleted source. Specifically, the eastern Tethys lags in response to ocean acidification compared to the rest of the global ocean. Understanding the differences between deep and shallow sea sites can help infer the carbon emission history and evaluate the carbon release mechanism that drives the PETM.

1. Introduction

While satellites, buoys, and weather towers provide concurrent measurements and observations about the effects of current climate change, future model projections must be improved so we understand how the planet will respond to a rapid increase in global temperatures from anthropogenic fossil fuel emissions. Although not a perfect analogy, largely because of the lack of ice sheets, the Paleocene-Eocene Thermal Maximum (PETM; ~56 Ma) is a worthy geologic event to compare and infer how modern Earth systems will respond to rapid carbon emissions (Kirtland Turner and Ridgwell, 2016; Meissner et al., 2014; Zachos et al., 2008). During the ~170,000-year event (Dunkley Jones et al., 2013; Zeebe and Lourens, 2019), 2,000-10,000 Pg C of ^{13}C -depleted carbon may have been released into the atmosphere-ocean system (Gutjahr et al., 2017; Kirtland Turner and Ridgwell, 2016; Zachos et al., 2005). This can explain perturbations to the global carbon cycle and the negative carbon isotope excursion (CIE) between 3-5‰ that is observed within the PETM records (Jones et al., 2019a; Keller et al., 2018; Zachos et al., 2008). Sea surface temperatures are also believed to have increased 5 to 9°C (Dunkley Jones et al., 2013; Inglis et al., 2020; Zachos et al., 2008), widespread benthic foraminifera extinction occurred (Alegret et al., 2021; Alegret et al., 2009), and poleward ecosystem migration took place (Smith et al., 2007; Wing et al., 2005).

To better understand the timing of the carbon injections and the climatic response, the PETM is broken into several stages. The event begins with the rapid CIE onset (between 1-5 kyr) when the carbon was released. Two CIE profiles have been proposed depending on a location and the examined substrate: a single emission pulse or multiple distinct pulses (Fig. 1). The $\delta^{13}\text{C}$ record reflects the PETM emission history, but incomplete records due to diagenesis, carbonate dissolution, bioturbation, or low sample resolution or sediment mixing of various nanoplankton components can lead to either interpretation of the CIE (Zhang et al., 2017). Following the CIE

is the “body phase” (between ~70-100 kyr) where $\delta^{13}\text{C}$ remained low and stable. The Early Eocene “recovery phase” (between ~50-100 kyr) shows $\delta^{13}\text{C}$ returning to pre-PETM values (Jones et al., 2019a). The recovery phase itself shows two distinct phases, with stage I occurring rapidly and stage II being more gradual (Stassen et al., 2012).

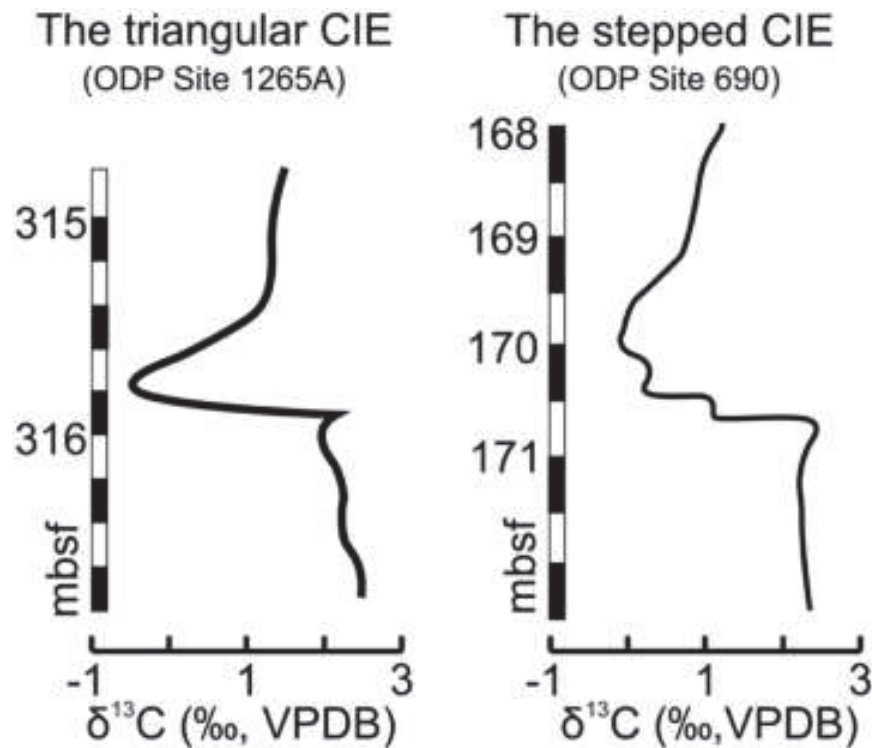


Figure 1: The two different CIE profiles during the PETM reflected in $\delta^{13}\text{C}_{\text{carb}}$. The singular pulse (left) is sampled at Integrated Ocean Drilling Project (IODP) Site 1265A at Walvis Ridge in the south Atlantic. The multiple emission scenario (right) shows a record from IODP Site 690 in Weddell Sea, Antarctica. Mbsf = meters below sea floor. VPDB = Vienna Peedee Belemnite, the international $\delta^{13}\text{C}$ standard. Borrowed from Westerhold et al. (2018).

Although the CIE is widely observed in both marine and terrestrial substrates, the source of the ^{13}C -depleted carbon is largely debated. Some argue it could be a result of a maximum in Earth's eccentricity (Lourens et al., 2005; Zeebe and Lourens, 2019), dissociation of methane hydrates (Dickens et al., 1997; Ruppel and Kessler, 2017), thermogenic methane (Frieling et al., 2019), a bolide impact (Fung et al., 2019; Schaller et al., 2019), or a combination of origins. The North Atlantic Igneous Province (NAIP) is believed to be coincident in time with the PETM and is another mechanism worthy of further investigations (Gutjahr et al., 2017; Svensen et al., 2010). The second of its two volcanic phases released $5\text{-}10 \times 10^6 \text{ km}^3$ of magma and opened the northeast Atlantic Ocean basin (Jones et al., 2019b). Mercury anomalies and mercury to total organic carbon (TOC) ratios in the North Sea and Dabibiya, Egypt show that localities near the NAIP record these volcanic signals in high concentrations (Jones et al., 2019a; Keller et al., 2018). Ash layers in close proximity to the NAIP from the North Sea (Stokke et al., 2021; Stokke et al., 2020b), Fur, Denmark (Jones et al., 2019a), Spitsbergen, Norway (Charles et al., 2011), and the North Atlantic (Saunders, 2016) additionally support the coincidence of timing of the NAIP and the PETM.

Regardless the carbon source, the copious amounts of carbon dioxide (CO_2) in the atmosphere lead to significant ocean acidification (OA) evidenced by negative excursion in boron isotopes of marine calcifiers (Babila et al., 2022; Penman et al., 2014). As a result, the calcite compensation depth (CCD) is believed to have shoaled, explaining why some deep ocean sites, like Walvis Ridge in the southeast Atlantic (Zachos et al., 2005) and remote locations in the central Pacific (Griffith et al., 2015), are missing sediment due to dissolution and replaced with terrigenous clay (Babila et al., 2018; Kump et al., 2009; Stokke et al., 2020a). However, despite OA being a global phenomenon during the PETM, the Atlantic Ocean experienced more

severe effects of OA compared to the Pacific, as evident of the 2 km versus a few hundred meter shoaling of the CCD (Zachos et al., 2005; Zeebe et al., 2009). Collectively, boron isotopes ($\delta^{11}\text{B}$) and modeling results indicate that pH decreased ~ 0.3 units (Babila et al., 2018; Gutjahr et al., 2017; Penman et al., 2014). The recovery process is believed to have taken ~ 100 kyr (Zachos et al., 2005), as a result of silicate weathering and organic carbon burial.

While many of these Earth system feedbacks have been studied in deep ocean or high latitude sites, there is a disproportionate representation of low latitude and shallow marine environments (Jaramillo et al., 2010; Li et al., 2020; Tian et al., 2021). Such understudied regions can lead to incorrect assumptions about the shape of the CIE (Kirtland Turner and Ridgwell, 2016). The subtropical, shallow eastern Tethys is an understudied region that was essential for heat and moisture exchange during the PETM. Both the eastern and western Tethys underwent rapid transgression-regression cycles and showed anoxic and euxinic conditions (Cao et al., 2018; Jiang et al., 2018; Remmelzwaal et al., 2019; Stokke et al., 2020a). However, despite the known effects of OA in the global oceans, it has yet to be investigated in the eastern Tethys.

Using an Earth system model of intermediate complexity, this study will investigate the time-varying $\delta^{13}\text{C}$ signature of the emitted carbon and the rates of carbon emission and sequestration during the PETM and evaluate the NAIP as a driver for the PETM. Specifically, the biogeochemistry of the global ocean will be explored, with emphasis on the eastern Tethys, which could have responded more severely to OA due to its known behavior as a carbon sink (Carmichael et al., 2017; Schulte et al., 2011) and its carbonate platform.

2. Methods

The carbon centric Grid Enabled Integrated Earth system model (cGENIE) is of intermediate complexity (Kirtland Turner and Ridgwell, 2016) and couples a 3D dynamic-

thermodynamic ocean model (36×36 grid, 16 vertical levels) with a 2D moisture and energy balance atmosphere model. The climate model has the capability to measure biogeochemical cycling of elements, stable carbon isotopes, marine sediments, and continental weathering (Adloff et al., 2020; Gutjahr et al., 2017; Ridgwell and Schmidt, 2010). A user configuration file detailed code that configured the bathymetry, paleogeography, planetary albedo, and wind fields to the early Eocene (55 Ma). Furthermore, this configuration portrays an ice-free world of the late Paleocene.

Following Gutjahr et al. (2017), an initial, closed system, spin-up (20 kyr) puts the model into a steady state. This first spin-up is a closed box model that does not allow input or output into the system and takes about ~20 kyr to achieve equilibrium. This run equilibrated the atmospheric CO₂ to 830 ppm and the $\delta^{13}\text{C}_{\text{atm}}$ value to -6‰. Afterwards, a second, open system spin-up (200 kyr) allowed an open box model to account for inputs and outputs. This spin-up takes a minimum ~100 kyr and accounts for natural processes that are not always in equilibrium, like weathering, volcanic outgassing, riverine input, and carbonate burial in the marine sediments. The second spin-up additionally defines the climatic and ocean circulation conditions of the PETM.

“Double-inversion” experiments were conducted to determine the time-varying $\delta^{13}\text{C}$ values of the emitted carbon source and the climatic impacts to the eastern Tethys throughout the PETM. These experiments require two forcing files which are applied onto the surface ocean of the model. The first forcing file contains boron isotopes ($\delta^{11}\text{B}$), a proxy for pH reconstruction. This data is presented in Gutjahr et al. (2017) and was collected from Integrated Ocean Drilling Program (IODP) site 401 in the deep, northeast Atlantic Ocean. The authors argue that the pH changes in the Atlantic can be represented unanimously for the globe. The second forcing file

contains carbon isotopes of bulk carbonates ($\delta^{13}\text{C}_{\text{carb}}$) that were collected from the eastern Tethys in Jiang et al. (in prep). A locally estimated scatterplot smoothing (loess) fit was applied to the $\delta^{13}\text{C}_{\text{carb}}$ data by determining a polynomial regression between consecutive data points. This process smooths the data and was conducted in the R programming language using function “loess” with a span parameter value of 0.2. Overall, the loess fit helps avoid mathematical instability in the model by avoiding large fluctuations in the forcing file. Both $\delta^{11}\text{B}$ and $\delta^{13}\text{C}$ were forced onto the surface ocean to diagnose the carbon emission flux and associated time-varying $\delta^{13}\text{C}$ values of the carbon sources.

A total of six experiments used the climate conditions in the spin-ups as a starting point and ran for 560,000 years to explore the onset, plateau, and recovery phases of the PETM and the post-PETM phase. Table 1 summarizes the key modeling results in each experiment. The experiment naming schemes represent the confidence limits of 2.5% and 97.5% of the pH reconstruction based on boron isotopes for the low and high pH scenarios, respectively (Gutjahr et al., 2017) (LO, MED and HI scenario). Three experiments include diagnosed flux of organic carbon burial (OCB) during the recovery phase of the PETM (i.e., 72.5 kyr from the onset of the PETM), and are named with OCB for each pH scenarios. It is believed that the burial of ~2,000-4,500 Pg C of organic carbon may have aided in the recovery phase of the PETM (Bowen and Zachos, 2010; Clarkson et al., 2021; Gutjahr et al., 2017; Penman and Zachos, 2018). As such, the OCB experiments explore the nature of the recovery process.

Table 1: cGENIE experimental descriptions

Experiment	Experiment Assumptions				Peak emissions (Pg/yr)	Cumulative Emissions	ΔSST	Peak excess weathering (PgC)
	pH range	Weathering?	Corg burial?	Mean δ ¹³ C (‰)				
DePalma_PETM_LO	7.296 – 7.704	YES	NO	-11.23	1.38	36,363	6.11	0.00208
DePalma_PETM_MED	7.464-7.732	YES	NO	-9.39	0.66	18,460	3.79	0.00194
DePalma_PETM_HI	7.570-7.741	YES	NO	-14.07	0.33	8,500	2.56	0.00186
DePalma_PETM_Corg_LO	7.296 – 7.704	YES	YES	-16.49	1.38	61,792	6.11	0.00208
DePalma_PETM_Corg	7.464-7.732	YES	YES	-19.26	0.66	42,553	3.79	0.00194
DePalma_PETM_Corg_HI	7.570-7.741	YES	YES	-23.83	0.33	34,324	2.56	0.00186

3. Results

3.1 Cumulative carbon emission, emission rate, atmospheric $p\text{CO}_2$, and time-varying $\delta^{13}\text{C}$ values

All six scenarios show that carbon was released in at least two distinctive pulses, with the larger pulse emitted 45 kyr after the onset of the CIE. The first pulse is released at a maximum rate of 1.4 Pg C yr^{-1} , $0.66 \text{ Pg C yr}^{-1}$, $0.33 \text{ Pg C yr}^{-1}$, for the low and low OCB, medium and medium OCB, and high and high OCB scenarios, respectively (Fig. 2). The cumulative amount of carbon released over the duration of the 560,000 years that is needed to match both the $\delta^{13}\text{C}$ and pH forcings range from 8,500 Pg C (high pH scenario) to 61,800 Pg C (low pH OCB) (Fig. 3). At 45 kyr, coincident with the first carbon emission pulse, the total amount of carbon sharply increases in all the experiments. All OCB scenarios release more carbon than the experiments without organic carbon burial because these experiments are accounting for additional carbon through the particulate organic carbon cycle whereas the non-OCB experiments do not.

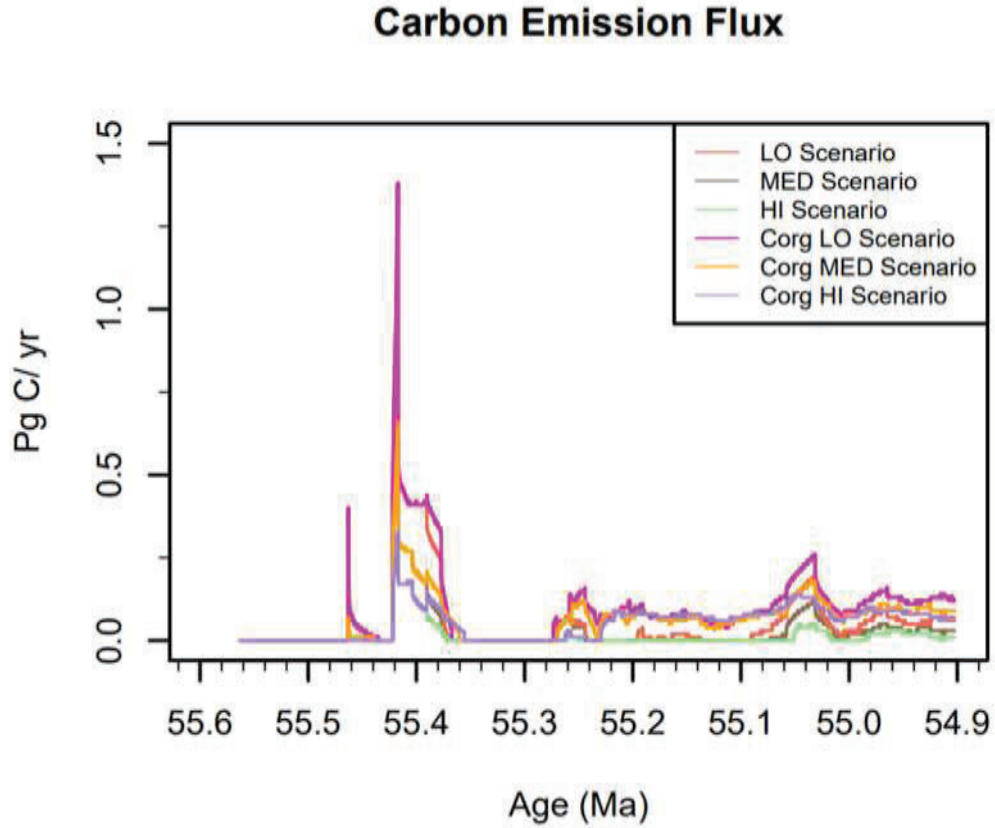


Figure 2: Carbon emission rate across the PETM of the low (red), medium (brown), high (green), low OCB (pink), medium OCB (orange), and high OCB (purple) scenarios. Note the two distinct carbon emission pulses.

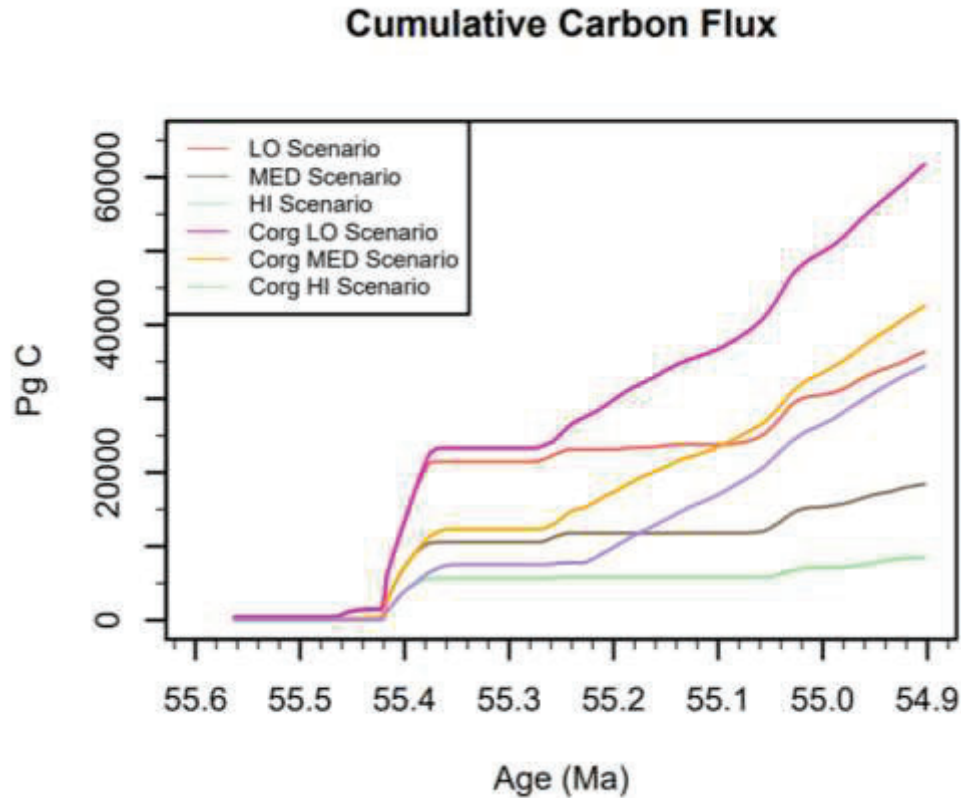


Figure 3: Cumulative emitted carbon for each experiment across the CIE onset, the PETM, PETM recovery, and the post-PETM.

The modeled atmospheric $p\text{CO}_2$ is widely different depending how much carbon is released. The $p\text{CO}_2$ begins at 834 ppm, 863 ppm, and 998 ppm for the high and high OCB, medium and medium OCB, and low and low OCB scenarios, respectively. The varying $p\text{CO}_2$ is a result of more carbon being released at the beginning of the low scenarios in comparison to the high experiments, where carbon is not released until ~ 40 kyr after the start of the CIE. The maximum concentration occurs ~ 45 kyr after the CIE with 4,080 ppm (low and low OCB), 2,175 ppm (medium and medium OCB), and 1,506 ppm (high and high OCB). Atmospheric $p\text{CO}_2$ then rapidly declines, but a smaller peak appears ~ 430 kyr after the CIE where concentrations reach 2,103 ppm (low), 2,102 ppm (low OCB), 1,430 ppm (medium), 1,429 ppm (medium OCB),

1,056 (high scenario), 1,049 ppm (high OCB) (Fig. 4). Despite $p\text{CO}_2$ decreasing by the end of the experiments, they remain significantly higher in comparison to the beginning concentrations.

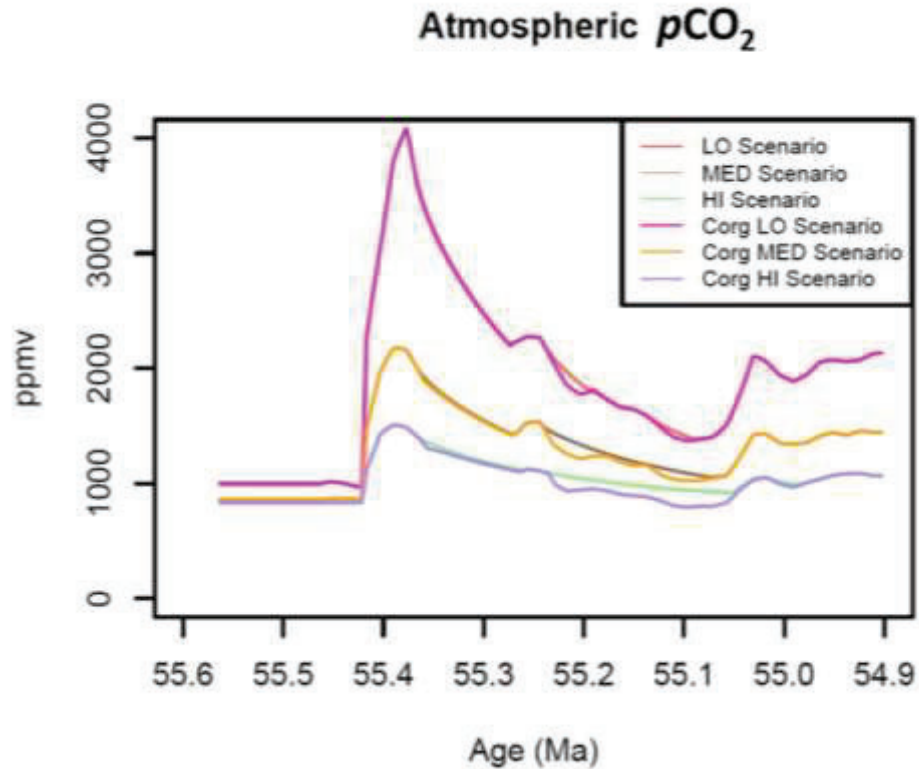


Figure 4: Atmospheric carbon dioxide concentration across the CIE onset, the PETM, the recovery phase, and the post-PETM.

The time-varying $\delta^{13}\text{C}$ values of the CO_2 sources depict the isotopic signature of the emitted carbon, providing insight on the temporal evolution of the ^{13}C -depleted sources. Numerical values equaling -100 and -999.999 were removed from the dataset as no known source can produce an isotopic signature with such low values. The results show that at ~45 kyr after the CIE onset the first $\delta^{13}\text{C}$ pulse quickly becomes lower (Fig. 5). Additionally, there are two short periods when there is no carbon emission flux. At ~250 kyr after the CIE, the second

pulse is observed with $\delta^{13}\text{C}$ ranging from $\sim -50\text{‰}$ to -26‰ and average $\delta^{13}\text{C}$ values between -24.0‰ to -6.9‰ , depending on the experiment. It should be noted that only the low scenario does not have carbon released during the second emission pulse. The $\delta^{13}\text{C}$ flux continues to remain within this range, indicating a slower emission rate with lower $\delta^{13}\text{C}_{\text{source}}$ values. Table 2 depicts the minimum, maximum, and average $\delta^{13}\text{C}$ values for each experiment for both carbon emission pulses. The results show an average $\delta^{13}\text{C}$ value of -22.6‰ to -7.9‰ for the first emission pulse whereas the second carbon emission pulse shows average $\delta^{13}\text{C}$ values between -24.0‰ to -6.9‰ .

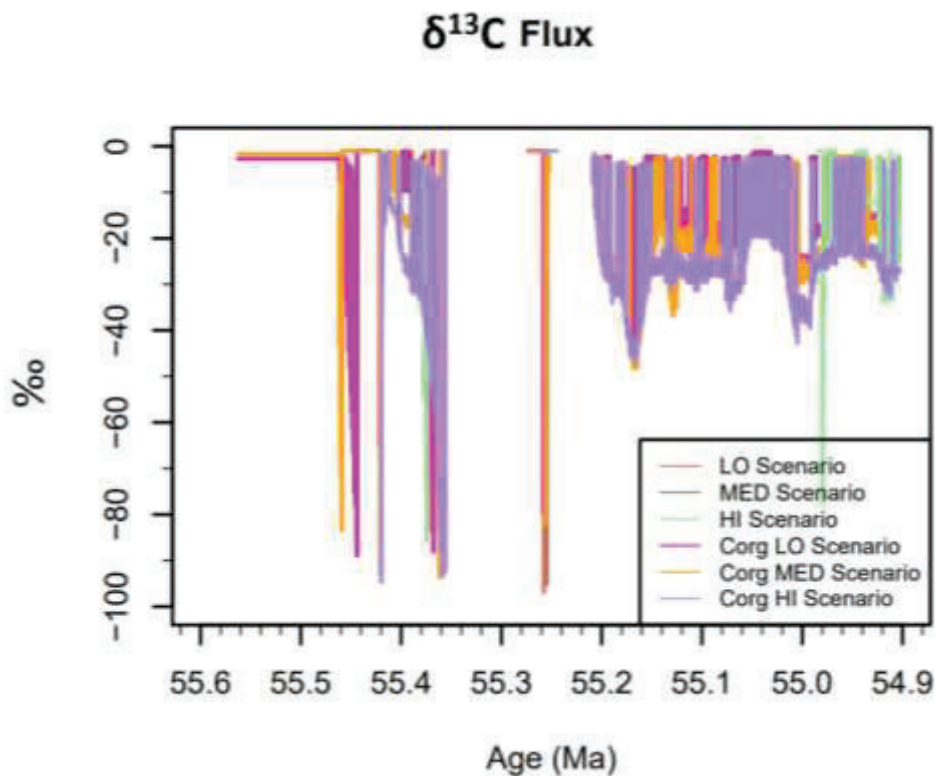


Figure 5: The $\delta^{13}\text{C}$ flux of the various experiments provides insight on the $\delta^{13}\text{C}_{\text{source}}$. Note the two distinct pulses and their varying $\delta^{13}\text{C}$ signature.

Experiment Name	First Pulse			Second Pulse		
	Maximum (‰)	Minimum (‰)	Average $\delta^{13}\text{C}$ (‰)	Maximum (‰)	Minimum (‰)	Average $\delta^{13}\text{C}$ (‰)
Low	-1.1	-35.7	-7.9	--	---	--
Medium	-1.1	-54.6	-14.4	-1.1	-11.1	-6.9
High	-1.0	-85.7	-22.6	-1.0	-77.8	-11.8
Corg Low	-1.1	-33.4	-10.4	-1.1	-43.8	-17.4
Corg Medium	-1.1	-37.5	-15.8	-2.2	-48.2	-21.3
Corg High	-1.1	-44.1	-20.8	-1.5	-46.9	-24.0

Table 2: The maximum, minimum, and average $\delta^{13}\text{C}$ value for both carbon emission pulses in each experiment. The average $\delta^{13}\text{C}$ provides insight on the $\delta^{13}\text{C}$ source.

3.2 Warming and acidification of the global ocean

The multiple carbon emissions had severe impacts and are reflective in the geochemistry of the global ocean. As a result of the rapid global warming, sea surface temperatures (SST) increased $\sim 2^\circ\text{C}$ (high and high OCB), 4°C (medium and medium OCB), and 6°C (low and low OCB) (Fig. 6). While the medium and high scenarios reached and sustained their maximum temperatures 75 kyr after the CIE, the low scenarios did not reach their highest temperature until 85 kyr after the CIE.

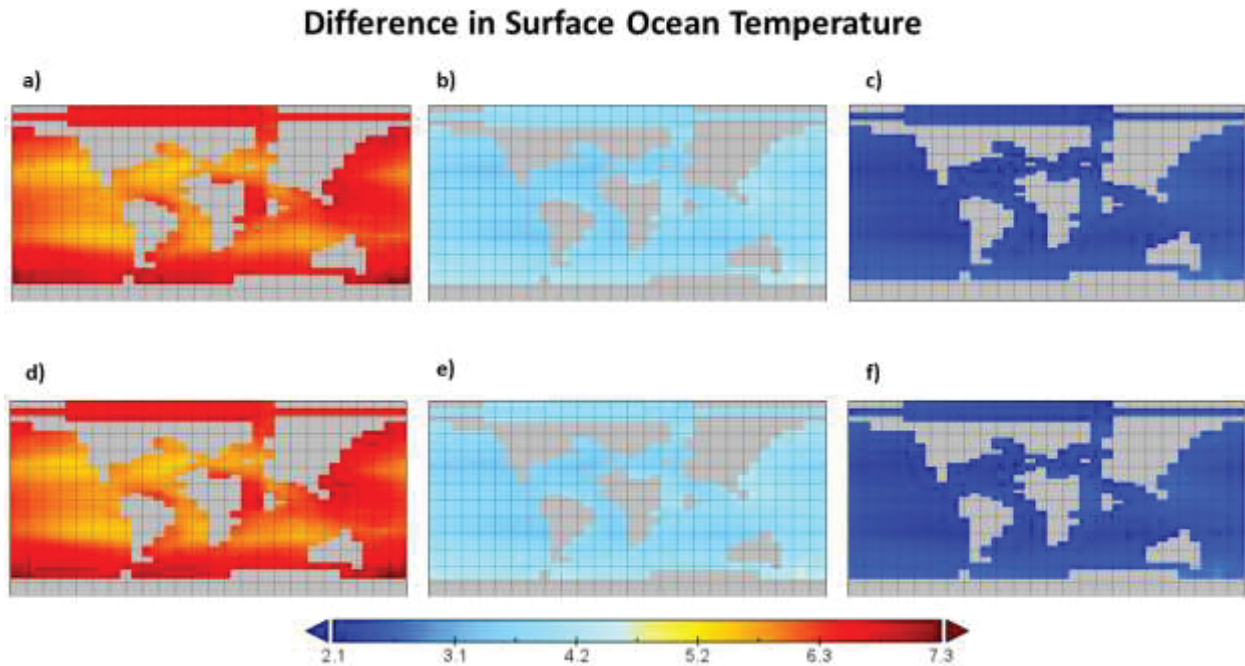


Figure 6: Temperature differences between the point of maximum temperature minus 100.5 years after the CIE A) Low scenario, with the maximum temperature reached at 85 kyr; B) Medium scenario, with the maximum temperature attained at 80 kyr; C) High scenario, with the maximum temperature obtained at 75 kyr.; D) Low OCB scenario, with the maximum temperature reached at 85 kyr; E) Medium OCB, with the maximum temperature attained at 80 kyr; F) High OCB, with the maximum temperature reached at 75 kyr.

The ocean-atmosphere flux can be observed with $\delta^{13}\text{C}_{\text{DIC}}$. Each scenario begins with $\delta^{13}\text{C}_{\text{DIC}} = 2.6\text{‰}$ and reaches its minimum values between -1.6‰ (low OCB) to -0.9‰ (high scenario) at ~ 90 kyr and ~ 205 kyr after the CIE, respectively (Fig. 7). The recovery pattern is vastly different depending on the experiment, with the OCB scenarios having a sharp increase in $\delta^{13}\text{C}_{\text{DIC}}$ once the carbon burial is initiated. In comparison to the low and medium scenarios, the

high pH experiment recovery path includes much higher $\delta^{13}\text{C}_{\text{DIC}}$ values. However, despite the different patterns, all scenarios end with $\delta^{13}\text{C}_{\text{DIC}} = 1.8\text{‰}$.

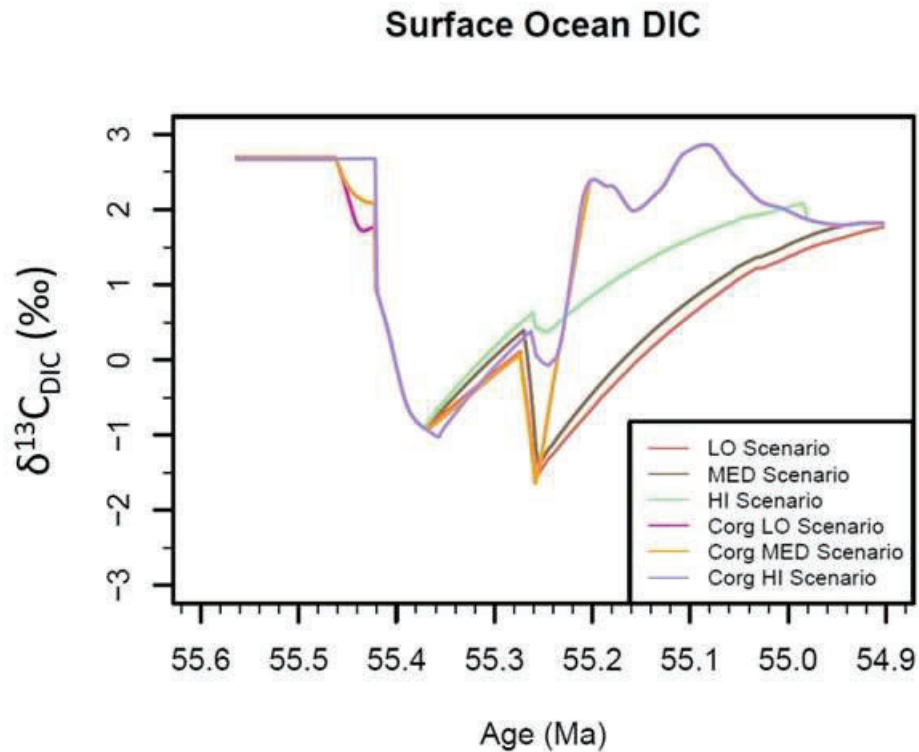


Figure 7: Surface ocean $\delta^{13}\text{C}_{\text{DIC}}$ across 560,000 years between the six experimental scenarios.

The sea-air gas exchange, which determines the amount of dissolved gases the surface ocean absorbs, also led to acidification, with some regions experiencing the effects more. The pH levels started at 7.67, 7.73, and 7.74 and dropped a total of ~ 0.4 , ~ 0.3 , and ~ 0.2 units, reaching their lowest values at ~ 80 kyr from the CIE onset for the low, medium, and high scenarios, respectively (Fig. 8). However, some regions experience OA effects more than others (Fig. 9). This correlates to a 134% difference in $[\text{H}^+]$ for the low and low OCB scenarios, an 86% difference in $[\text{H}^+]$ for the medium and medium OCB, and a 50% difference in $[\text{H}^+]$ for the high

and high OCB. It should be noted that pH is measured on a logarithmic scale, hence the large percent changes. The percent differences were calculated from the two equations below:

$$\text{pH} = -\log [\text{H}^+]$$

$$\text{Percent difference} = \frac{\text{new pH} - \text{initial pH}}{\text{initial pH}} * 100$$

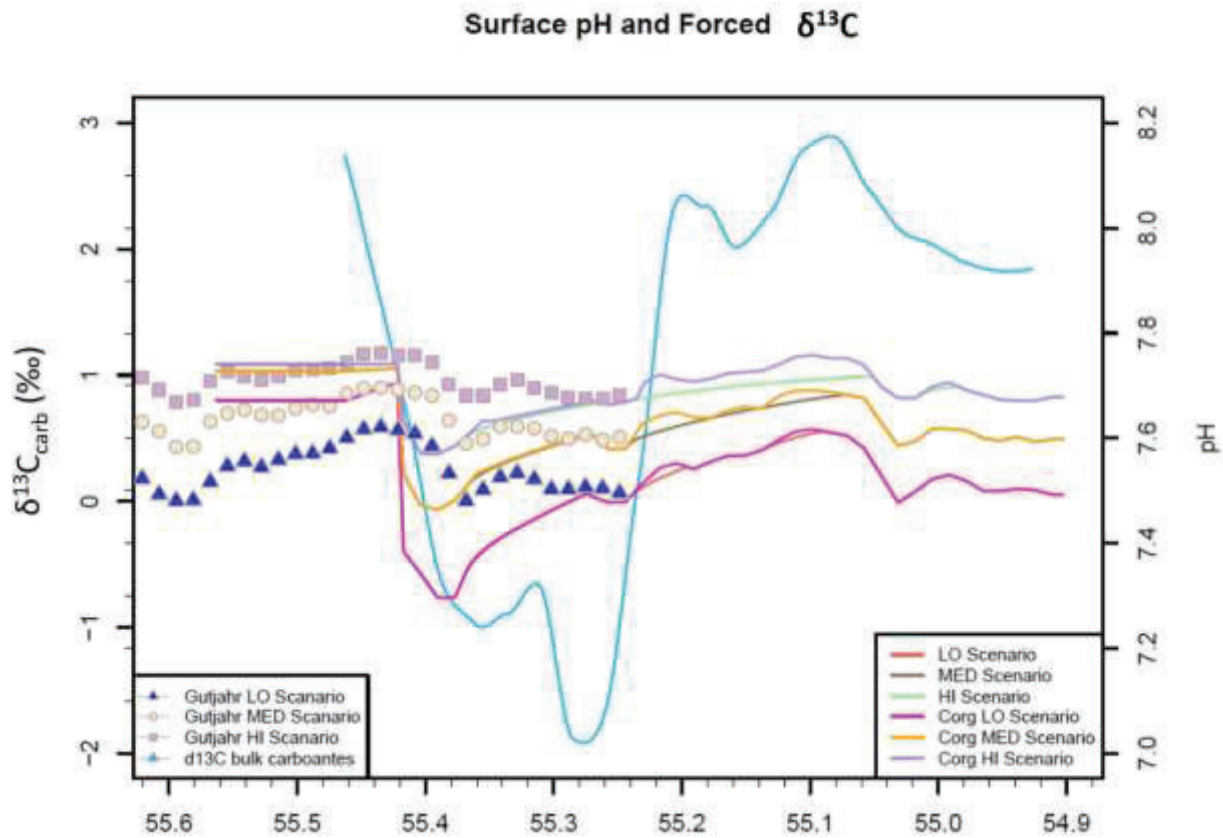


Figure 8: The eastern Tethys $\delta^{13}\text{C}_{\text{carb}}$ forcing (blue line) and the pH forcings for the high, medium, and low scenarios, represented as squares, circles, and triangles, respectively. The model's calculated pH fluctuations for each experiment are denoted with the colored

curves.

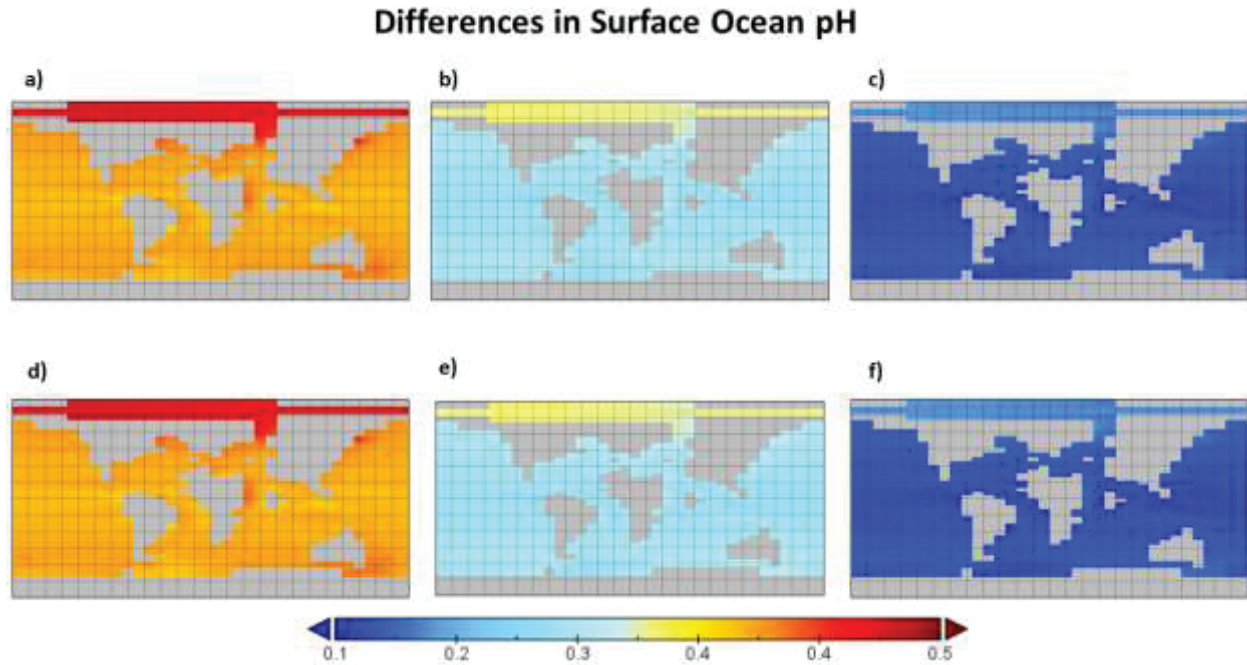


Figure 9: The pH differences of the point of lowest pH minus 100.5 years after the CIE. A) Low scenario, with the lowest pH at 85 kyr; B) Medium scenario, with lowest pH at 80 kyr; C) High scenario, with the lowest pH at 75 kyr; D) Low OCB scenario, with the lowest pH at 85 kyr; E) Medium OCB scenario, with the lowest pH at 80 kyr; F) High OCB scenario, with the lowest pH at 75 kyr.

As a result of the OA, the carbonate (CaCO_3) saturation state decreases, which can be measured with two polymorphs of calcium carbonate, calcite and aragonite, with calcite being less soluble and more likely to be preserved in sediments than aragonite (Sulpis et al., 2022). The carbonate saturation state can be measured as such:

$$\Omega_{\text{Calcite}} = \frac{[\text{Ca}^{2+}][\text{CO}_3^{-2}]}{K_{sp}}$$

where K_{sp} is the solubility product constant of CaCO_3 . When $\Omega > 3$, CaCO_3 forms; however, when $\Omega < 1$, CaCO_3 dissolves due to undersaturation. The modeling results show that the lowest benthic Ω_C values occur 45 kyr after the CIE onset and start to recover at 90 kyr. The differences in benthic Ω_C range from 0.15 (high and high OCB) to 1.2 (low and low OCB), while surface Ω_C differ between 0.35 (high and high OCB) to 1.4 (low and low OCB) (Figs. 10-11). The largest Ω_C differences correspond to the shallow marine environments in the eastern Tethys, the western Tethys near the European plate, the eastern Indian plate, and central northern Africa (Fig. S1). Meanwhile, the global deep sea shows less change in benthic Ω_C , with the Atlantic having more dissolution than the Pacific.

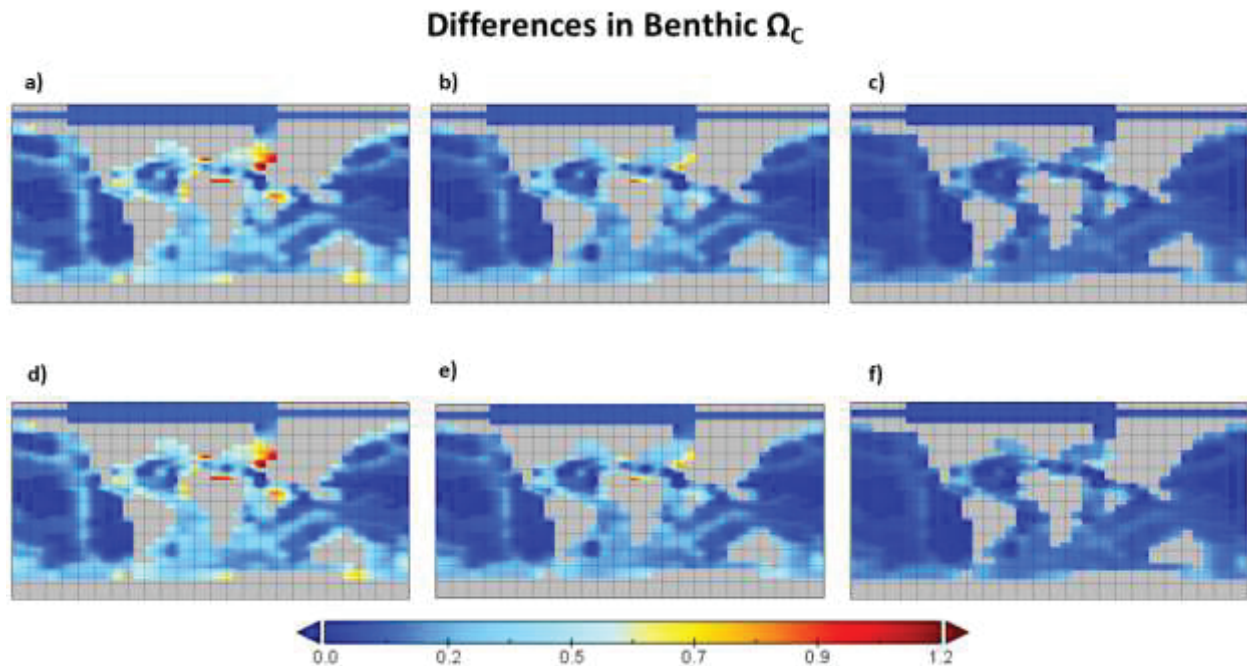


Figure 10: The differences in benthic Ω_C is calculated between the point of lowest concentration (45 kyr) and the start of the recovery time (90 kyr). A) The low scenario; B) The medium scenario; C) The high scenario; D) The low OCB scenario; E) The medium OCB scenario; F) The high OCB scenario.

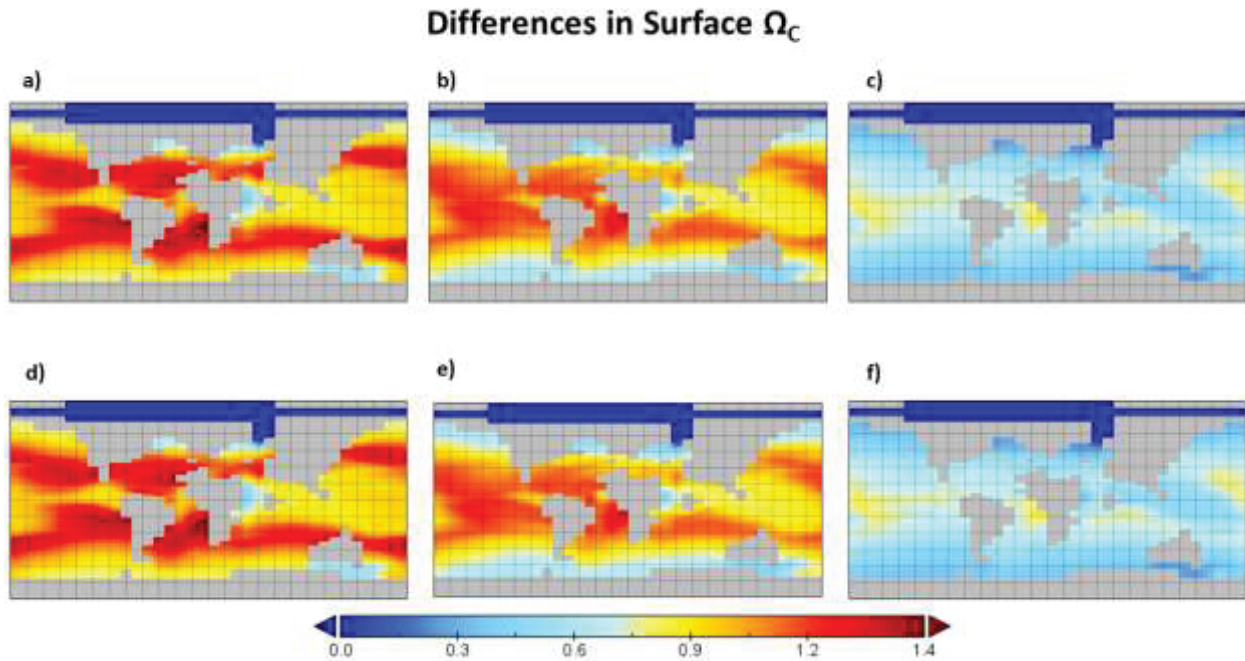


Figure 11: The differences in surface Ω_C is calculated between the point of lowest concentration (45 kyr) and the start of the recovery time (90 kyr). A) The low scenario; B) The medium scenario; C) The high scenario; D) The low OCB scenario; E) The medium OCB scenario; F) The high OCB scenario.

At the start of the CIE, average surface ocean dissolved oxygen (O_2) concentrations were $2.12 \times 10^{-4} \mu\text{mol/kg}$ and are the lowest between $\sim 30^\circ\text{N}$ and $\sim 30^\circ\text{S}$. There are little differences in dissolved O_2 between the OCB scenarios and their respective pH experiments. By 85 kyr, minimum dissolved oxygen expands to $\sim 45^\circ\text{N}$ and $\sim 45^\circ\text{S}$ and reaches its lowest values between $2.06 \times 10^{-4} \mu\text{mol/kg}$ (high and high OCB) to 1.98 to $2.06 \times 10^{-4} \mu\text{mol/kg}$ (low and low OCB). All scenarios begin to recover by ~ 90 kyr. The expansion of the minimum dissolved O_2 zones correspond to point of highest temperatures, which is likely a result of decreased gas solubility (Remmelzwaal et al., 2019). The increased temperature in the low and high scenarios (6°C and

2°C, respectively) explains the differences in dissolved O₂ in the Arctic and southeast Australia and Antarctica.

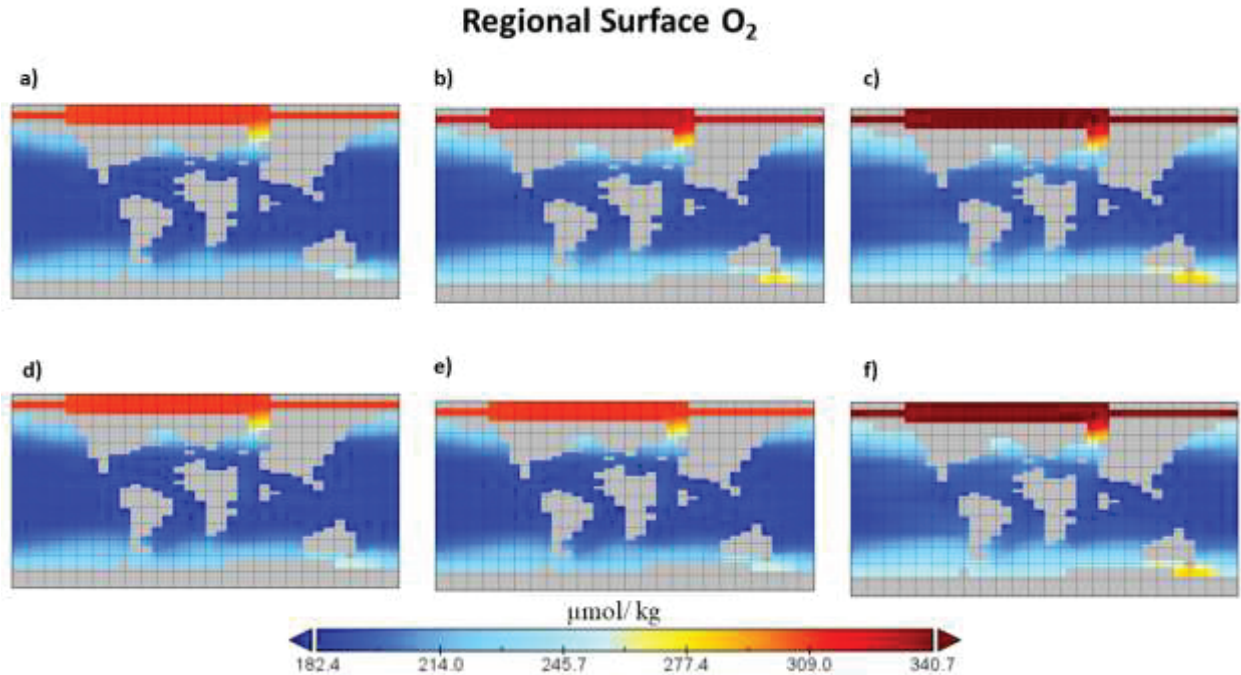


Figure 12: The lowest point of dissolved surface ocean O₂ A) The low scenario, at 85 kyr; B) The medium scenario, at 80 kyr; C) The high scenario, at 75 kyr; D) The low OCB scenario, at 85 kyr; E) The medium OCB scenario, at 80 kyr; F) The high OCB scenario, at 75 kyr

Benthic hypoxia and anoxia levels have additionally been observed during the PETM. Hypoxic conditions are achieved when dissolved O₂ concentrations are < 63 μmol/kg whereas anoxia occurs when O₂ concentrations equal 0 μmol/kg (Breitburg et al., 2018; Kapetanaki et al., 2020). Our model results show a sharp decrease in dissolved O₂ at ~45 kyr after the CIE where O₂ levels reach a minimum of 55.2 μmol/kg (low and low OCB), 78.4 μmol/kg (medium and medium OCB), and 107.1 μmol/kg (high and high OCB) (Fig. 13). Dissolved O₂ also decreases during the second carbon emission pulse, but the model results show a minimum decrease to

128.3 $\mu\text{mol/kg}$. Organic carbon burial is initiated 72.5 kyr after the start of the CIE and at this point the OCB scenarios begin to differentiate and fluctuate compared to the non-OCB experiments.

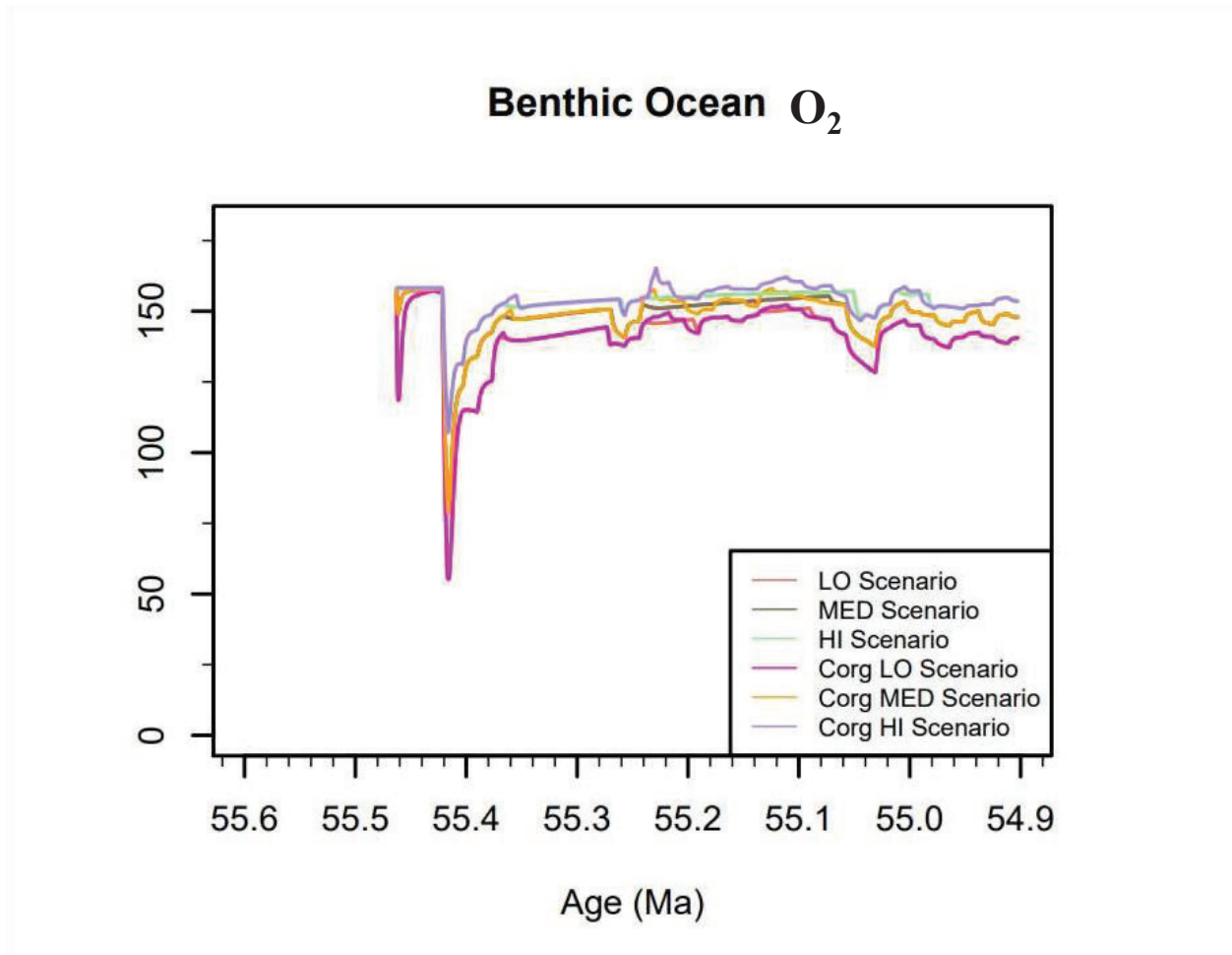


Figure 13: The averaged dissolved benthic O_2 concentrations for the six experiments.

Hypoxic conditions are reached when $\text{O}_2 < 63 \mu\text{mol/kg}$. Note the sharp decreases in dissolved O_2 occurs the time as the carbon emission pulses.

3.3 Organic carbon burial and the PETM recovery

It has been previously noted that silicate weathering and OCB have aided in the recovery of the PETM by burying $\sim 2,000$ - $4,500 \text{ Pg}$ of organic carbon (Bowen and Zachos, 2010;

Clarkson et al., 2021; Gutjahr et al., 2017; Penman and Zachos, 2018). Beginning 72.5 kyr after the CIE, the model will remove organic carbon from the surface ocean when the modeled $\delta^{13}\text{C}$ is less than the $\delta^{13}\text{C}_{\text{carb}}$ forcing. The results show OCB occurs immediately 72.5 kyr after the CIE, indicating that organic carbon is buried and aids in the recovery of the first carbon emission pulse (Fig. 14). The results additionally show a sharp increase during the second carbon emission pulse before plateauing. The model output shows that a total of 25.7, 24.6, and 27.1 Eg C of organic carbon buried for the low, medium, and high OCB scenarios, respectively (Fig. 15).

The results additionally indicate an average $\delta^{13}\text{C}$ of -29.5‰, -29.0‰, and -28.3‰ for the low, medium, and high OCB experiments, respectively (Fig. 16). There is an interval of time during the scenarios (~108- 226 kyr after the CIE) when there is no carbon emissions and no carbon burial. The model output reported $\delta^{13}\text{C}$ values of -100 and -999.999, and similar to the $\delta^{13}\text{C}$ flux, these values were removed from the dataset because no known source is believed to produce an isotopic signature with such low values. Table 3 summarizes the results of the OCB experiments.

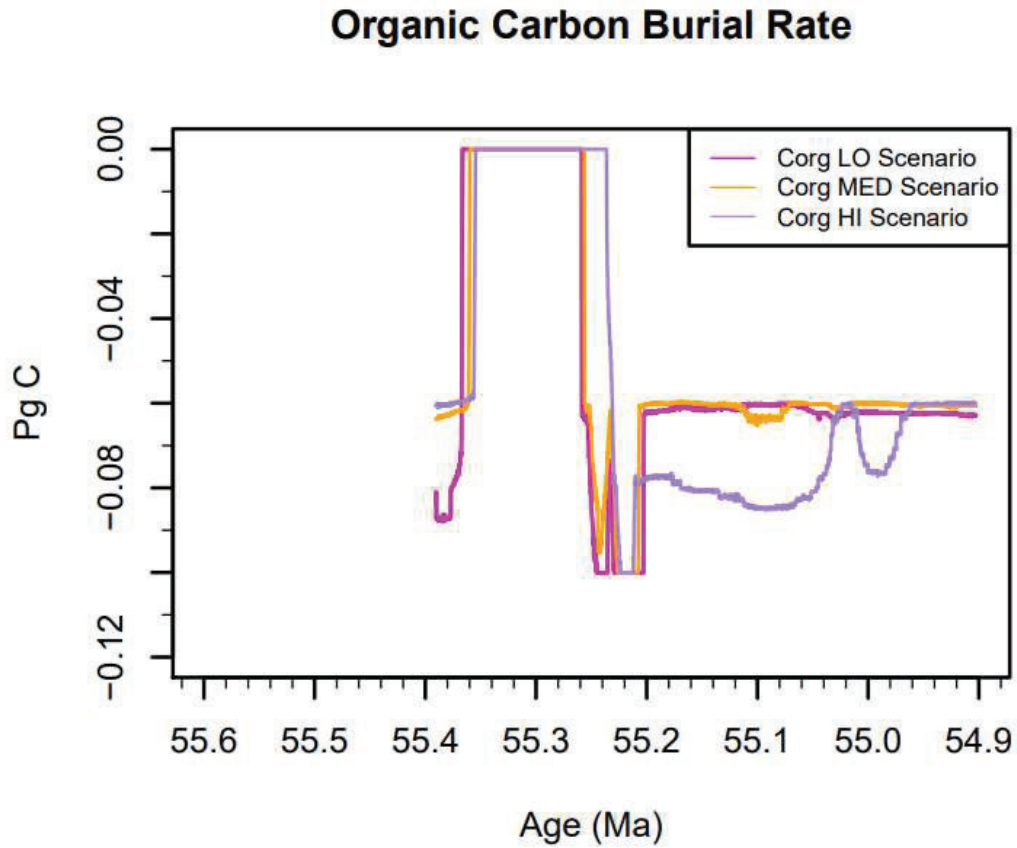


Figure 14: The organic carbon burial rate. cGENIE simulates OCB when the model $\delta^{13}\text{C}$ is lower than the $\delta^{13}\text{C}$ forcing file. Burial is initiated 72.5 kyr after the start of the CIE.

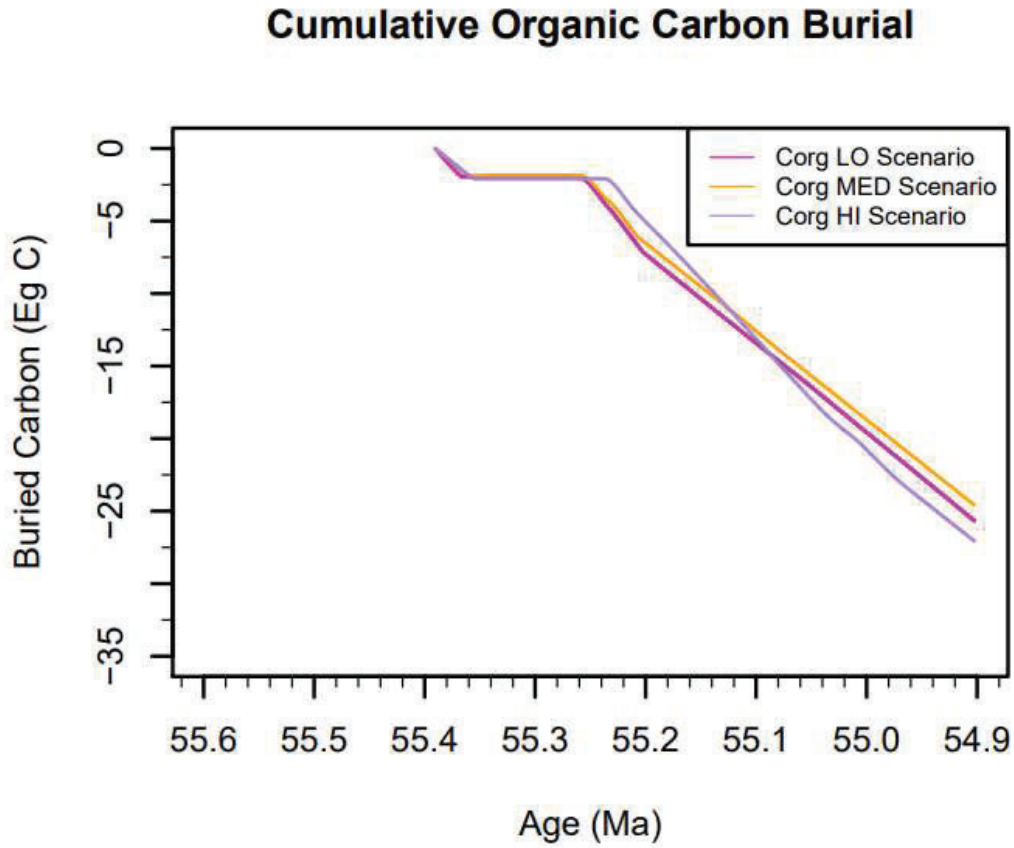


Figure 15: The cumulative buried carbon across 560,000 years. OCB is believed to help aid in the recovery of the PETM.

Cumulative Organic Carbon Burial Carbon Isotopes

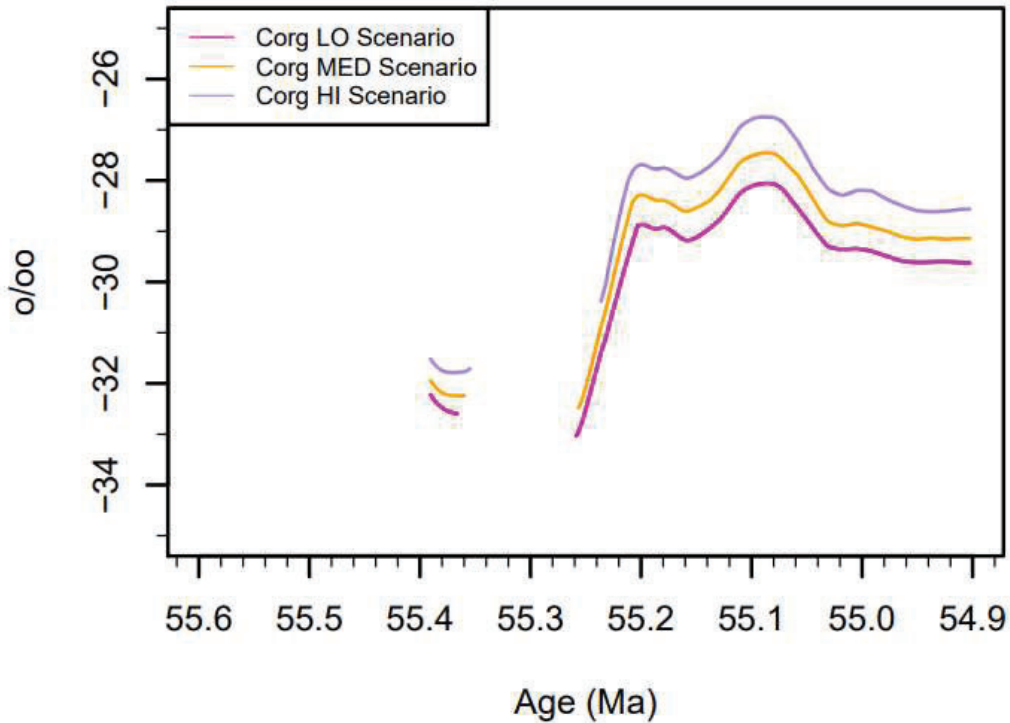


Figure 16: The average $\delta^{13}\text{C}$ for the buried organic carbon, beginning 72.5 kyr after the CIE.

Experiment Name	Total buried carbon (Eg C)	Average $\delta^{13}\text{C}$ (‰)
Low OCB	25.7	-29.5
Medium OCB	24.6	-29.0
High OCB	27.1	-28.3

Table 3: Organic carbon burial begins 72.5 kyr after the CIE. A summary of the total amount of carbon buried and the average $\delta^{13}\text{C}$ values for each OCB experiment.

4. Discussion

4.1 Determining the ^{13}C -depleted source

The atmospheric and oceanic effects of the PETM have been documented at various localities around the globe. Although some argue that there could have been 4-12 carbon pulses throughout the PETM (Frieling et al., 2017), the modeling results here suggest that there were two distinct pulses, with the first pulse being larger than the second. This is in agreement with other findings based on terrestrial and marine carbon isotope records (Bowen et al., 2015; Gutjahr et al., 2017). Other studies report that carbon was released at a rate between 0.2 to 1.7 Pg C yr⁻¹, but there is debate whether the emission was continuous or instantaneous (Bowen et al., 2015; Cui et al., 2011; Jones et al., 2019b). The cGENIE modeling results here support a rate no more than 1.5 Pg C first pulse, followed by a slower second pulse ~0.3 Pg C (Jones et al., 2019b).

The trigger for the PETM is widely debated, but each source has a distinct $\delta^{13}\text{C}$ signature. Since the results do not show an instantaneous release of carbon, bolide impact is unlikely to be the driver of the PETM (Fung et al., 2019; Schaller et al., 2019). Rather, the modeling results show that the $\delta^{13}\text{C}_{\text{source}}$ values are relatively low (-15‰ to -11‰), supporting a slow yet continuous degassing from mainly the NAIP (where $\delta^{13}\text{C}_{\text{mantle}} = -6\text{‰}$) that peaks ~45 kyr after the CIE. The warming that accompanied this release likely then caused feedbacks that later initiated the emissions for the second pulse, which has $\delta^{13}\text{C}_{\text{source}}$ values between ~ -25‰ to -50‰. Possible origins of this carbon can include organic carbon oxidation ($\delta^{13}\text{C} = -22\text{‰}$) (Frieling et al., 2016; Panchuk et al., 2008), permafrost thawing ($\delta^{13}\text{C} = -26\text{‰}$) (DeConto et al., 2012), or methane hydrates ($\delta^{13}\text{C} = -60\text{‰}$) (Dunkley Jones et al., 2010; Gutjahr et al., 2017). Previous studies have concluded that methane hydrates alone could not have caused the negative CIE (Cui and Schubert, 2018) because ocean waters would need to warm for at least 10,000

years to penetrate the top hundred meters of sediment to release the stored methane (Zeebe, 2013). However, the accompanied warming during the second carbon emission pulse is enough to explain the short SST increases, the decreased dissolved oxygen levels, and the increased $p\text{CO}_2$, hence further challenging the environmental stresses and Earth systems recovery.

4.2 Ocean acidification

The modeling results show that the entire global ocean became acidic following the initial carbon emission pulse, with high latitudes and pockets of ocean near the equator seeing the effects sooner and more severe. Additionally, the results show a region at $\sim 30^\circ\text{N}$ in the eastern Tethys and $\sim 45^\circ\text{N}$ off the coast of the Asian continent resisted acidification and recovered much sooner in comparison to the deep ocean and other shallow environments (Fig. S3). The eastern Tethys is the only site that shows higher benthic Ω_{C} values compared to the remainder of the global ocean, highlighting the uniqueness of this region. To confirm the model's large pH changes in the Arctic and the resistance of the eastern Tethys, it is recommended that pH reconstruction work is conducted in these locations and compared to the modeling results shown here.

The $\delta^{13}\text{C}_{\text{DIC}}$ values can be affected by the ocean-atmosphere CO_2 exchange, which determines the amount of carbon being absorbed in the surface ocean. Specifically, the exchange rate is dependent on temperature or if there is upwelling or mixing at a locality (Cheng et al., 2019; Kirtland Turner and Ridgwell, 2016; Wu et al., 2019). The high and high OCB scenarios are associated with the highest $\delta^{13}\text{C}_{\text{DIC}}$ values, consistent with their minimal OA effects and small changes in the $\delta^{11}\text{B}$ forcing.

Various sites around the globe show a pH difference of up to ~ 0.3 units, suggesting that regional pH heterogeneity exists for all scenarios but the high pH scenarios. The high pH

scenarios show no more than a 0.1 difference in pH regardless of the depth or SST. This emphasizes the spatial variability of the surface ocean pH and highlights the importance of collecting more pH data from other sites around the globe.

4.3 Temperature and its effects

Compared to other temperature reconstructions (Mg/Ca, TEX₈₆, $\delta^{18}\text{O}$), the $\sim 2^\circ\text{C}$ temperature difference of the high and high OCB experiments are too low of a change to be an accurate representation of the PETM. Although the $\sim 4^\circ\text{C}$ difference of the medium scenarios are within the calculated temperature reconstructions, it is a lower projection, while the $\sim 6^\circ\text{C}$ difference from the low and low OCB experiments are in agreement with other temperature reconstructions (Dunkley Jones et al., 2013; Zachos et al., 2008).

A rapid increase in temperature could have stressed surface ocean photosynthesizers, as demonstrated by their decreased test sizes (Frieling et al., 2017), although size increases in some foraminifera species have also been reported (Remmelzwaal et al., 2019). However, while open ocean productivity decreased, shelf productivity increased due to higher nutrient availability from coastal runoff and increased $p\text{CO}_2$ and temperature, resulting in increased metabolic rates (Gibbs et al., 2006; Pörtner et al., 2014; Scheibner and Speijer, 2008), which may have caused eutrophication in the eastern Tethys and other shelf regions (Remmelzwaal et al., 2019; Stokke et al., 2020a). Increased surface productivity could have led to anoxic bottom waters, contributing to the benthic foraminifera extinction (Alegret et al., 2021; Nagy et al., 2013; Tian et al., 2021). Studies show higher temperatures and a lack of adaptation are thought to be the main driver for the extinction of *Stensioeina beccariiiformis*, *Cibicidoides hyphalus*, *Nuttallinella florealis*, *Bolivinooides delicatulus*, *Bolivina inconspicua*, *Bulimina kulgeri*, and *Siphogenerinoides brevipinosa*, among many more species, with strong emphasis on local impacts rather than

universal effects in the global ocean (Alegret et al., 2021; Alegret et al., 2009; Takeda and Kaiho, 2007).

Despite the observed anoxic conditions in the eastern Tethys, our modeling results do not show lower regional hypoxic or anoxic conditions in the eastern Tethys or in upwelling zones off the coast of western South America and the western Indian plate (Rommelzwaal et al., 2019). Unlike Rommelzwaal et al. (2019), our experiments does not account for varying phosphate inventories, explaining the lack of regional hypoxic and anoxic differences. Previous work has also shown that the Pacific contains more dissolved O₂ than the Atlantic, which is also not observed within our experiments (Zhou et al., 2016).

4.4 Organic carbon burial and the PETM recovery

Double-inversion experiments provide an advantage in detailing how the climate recovered from the PETM. It is believed that the elevated global temperatures drove increased rates of silicate weathering, which aided in the pH recovery (Clarkson et al., 2021; Gutjahr et al., 2017; Penman, 2016). However, while our model results do account for the weathering flux, previous studies have noted this (Gutjahr et al., 2017).

Compared to the non-OCB scenarios, the OCB experiments show close agreement with the $\delta^{13}\text{C}$ recovery trend when the burial beginning 72.5 kyr after the CIE. The averaged $\delta^{13}\text{C}$ are at most 2.2‰ higher than Gutjahr et al. (2017), which found the average OCB $\delta^{13}\text{C} = -30.5\text{‰}$. Furthermore, the total amount of carbon buried after the significant peak in the OCB rate (Fig. 14) corresponds to the second carbon emission pulse. The total amount of buried carbon at this point ranges from ~4,000 Pg C (high OCB) to ~6,000 Pg C (low OCB). Gutjahr et al. (2017) found their model experiments buried an average of 2,500 Pg C, but our high OCB results agree more with the results from Clarkson et al. (2021), whose model results show ~4,900 Pg C were

buried and drove the recovery process. Our low OCB scenario shows ~1,000 Pg C more buried organic carbon compared to previous studies.

5. Conclusion

Based on the six cGENIE scenarios, we conclude that there were two distinct carbon emission pulses beginning at 55.93 Ma (Westerhold et al., 2018) with emissions reaching no more than 1.5 Pg C and 0.3 Pg C, respectively. The first pulse of $\delta^{13}\text{C}$ supports degassing from the NAIP which could have then created feedback loops triggering methane releases for the second pulse. The pH differences in the high and high OCB scenarios were not enough to match the sedimentary record highlighting the distinct pH responses in shallow and deep sea sites during the PETM.

Specifically, the eastern Tethys Sea shows resistance to OA and preserves saturated conditions with regards to benthic and surface carbonate Ω_{C} . Studying shallow marine and low latitude regions like the eastern Tethys highlights the spatial variability of such regions to rapid global warming events that were previously overlooked.

Chapter 2: New black carbon isotopes from the eastern Tethys during the PETM to investigate wildfire history

Abstract

The North Atlantic Igneous Province (NAIP) has been proposed as the trigger for the PETM and the initial source of the ^{13}C -depleted carbon emissions. As a result of the induced warming, wildfires were prominent in some regions due to warmer temperatures and changes in water availability and formed black carbon (BC), a product of incomplete combusted organic matter. The eastern Tethys is a region that allows exploration of how subtropical terrestrial ecosystems near shallow marine environments responded to the rapid global warming and carbon cycle perturbations. In this study, BC is extracted from the sedimentary record to investigate the site's wildfire history and hydrological cycle in response to the PETM. The results conclude that more moisture was delivered to the region, likely limiting the frequency of wildfires during the PETM and shifting the vegetation from gymnosperms to angiosperms. The presence of BC and clay content unevenly dispersed throughout the record suggests that rainfall was delivered during extreme, wet seasons during the PETM.

1. Introduction

In addition to changes in ocean chemistry and ecosystems, the changes in climate during the PETM caused significant regional impacts on land. The rapid warming caused poleward ecosystem migrations (Keller et al., 2018; Smith et al., 2007) and could have contributed to smaller and more diversified mammals (Abigail et al., 2017; Jaramillo and Cárdenas, 2013).

The higher temperatures also provided more energy to accelerate the hydrological cycle, impacting a region's total water availability. In combination with elevated CO₂ concentrations, this could have led to shifts in vegetation and biomes. While it is believed that some areas received more extreme, seasonal precipitation (Carmichael et al., 2017; Carmichael et al., 2018), other regions, like continental interiors, become drier (Kraus and Riggins, 2007). Evaporation rates were also higher in the tropics and subtropics due to warmer temperatures, which could have impacted ocean density and circulation (Carmichael et al., 2017; Zachos et al., 2003). Furthermore, long-chain *n*-alkanes from the Arctic show that some regions that had little moisture received increased water vapor delivery (Pagani et al., 2006). Increased precipitation and runoff in some localities can explain kaolinite deposits, a clay material from warm and humid environments, along continental margins (Kelly et al., 2005; McInerney and Wing, 2011; Stokke et al., 2021).

The altered hydrological cycle and temperatures have the potential to drastically change some landscapes. Palynological samples from the Jiangnan Basin in central China, a once continental, arid environment, received increased precipitation during the PETM, transforming the region into a diverse tropical and subtropical broadleaf forest (Xie et al., 2022). Similar features can be observed in southern Australia (Hurdeman et al., 2021) and South America (Jaramillo and Cárdenas, 2013). In fact, it is believed that heat tolerant, tropical plants expanded

and migrated northwards while diversifying (Jaramillo et al., 2010; Tipple et al., 2011). Likewise, palynological records from the Cap d'Ailly region of Normandy, France (Garel et al., 2013), the central North Sea near Scotland (Kender et al., 2012), the Arctic (Willard et al., 2019), and New Zealand (Handley et al., 2011) developed from restricted marshes in the late Paleocene to eutrophic swamps dominated by algae blooms during the PETM.

Changes in water availability and vegetation could have additionally contributed to wildfires. Increased abundance of black carbon (BC) and charcoal, products of the incomplete combustion of organic matter, have been observed in IODP Site 1210B Shatsky Ridge in the remote central Pacific, the New Jersey Atlantic margin, and Cobham, England (Baker, 2022; Collinson et al., 2007; Fung et al., 2019; Moore and Kurtz, 2008). The “wildfire hypothesis” of Paleocene peat deposits have previously been disproven to explain the global negative CIE, largely because BC abundance does not increase during the PETM and $\delta^{13}\text{C}_{\text{BC}}$ records signals of young, burned biomass as opposed to peat (Kurtz et al., 2003; Moore and Kurtz, 2008). However, regional wildfires likely happened to explain the occurrence of BC in the sedimentary records. Wildfires also seem to have persisted despite wetter conditions, as supported by increased polycyclic aromatic hydrocarbons (PAHs) abundance in the Arctic (Denis et al., 2017).

While the North Atlantic Igneous Province (NAIP) is argued to be the trigger for the PETM, it cannot be ignored that wildfires contributed a portion of the released carbon. Few studies have investigated paleofire archives in the sedimentary records and only one study has extracted BC during the PETM (Moore and Kurtz, 2008). This study aims at using BC as a proxy to reconstruct terrestrial paleo-environments from the Kuzigongsu (KZGS) section of the Tarim Basin in the eastern Tethys. The use of $\delta^{13}\text{C}_{\text{BC}}$ can determine how the eastern Tethys terrestrial ecosystems responded to the PETM, where previous work has only investigated the foraminiferal

and calcareous nannofossil responses (Cao et al., 2018; Jiang et al., 2018). Specifically, we explore the wildfire history at the KZGS section and investigate how vegetation and water availability changed, if at all, at the Tarim Basin.

2. Geologic Background

The Tarim Basin is located in the modern day northwest China and records a thick sequence of continental to shallow marine deposits that accumulated during the Paleozoic to the Cenozoic (Cao et al., 2018). The transition from the Mesozoic to the Cenozoic transformed the region from a continental basin to a restricted marine basin (Jiang et al., 2018). By the time of the PETM, the Tarim Basin was a warm semi-restricted seaway that connected the eastern Tethys and the western Mediterranean Tethys (Cao et al., 2018). The region was tectonically active and was surrounded by a carbonate platform (Cao et al., 2018; Jiang et al., 2018).

The Kuzigongsu (or KZGS) section is located 5 km northwest of Wuqia County (Uyghur Autonomous Region, China) and consists of 47.64 meters of fine-grained calcareous rocks of the Qimugen Formation. The PETM boundary is located between 19.89 - 30.5 m, as evident of the CIE in bulk carbonates and changes in the calcareous nannofossil biostratigraphy (Wang et al., in revision). A total of 480 samples were collected at ~10 cm intervals. A deepening of the water depth is evident from the Paleocene to Eocene transition. Facies analysis indicates a rapid rise in relative sea-level, allowing deposition of shallow-marine sediments (lagoonal to open-marine environments) of the Qimugen Formation over dolomite and gypsum layers of the Aertashi Formation (Jiang et al., 2018). The interval of interest, members I and II of the Qimugen Formation, comprises a sequence of carbonate mudstones, bioclastic wackestones, marlstones, siltstones, and shales (Fig. 17). The entire sequence is rich in bivalves, foraminifera, calcareous nannofossils, and ostracods, except for the levels of siltstones (9 – 22 m) where there is no

evidence of macro-fossils, and the biostratigraphy shows an almost total absence of calcareous nanofossils, suggesting a period of ocean acidification (Jiang et al., 2018). The foraminiferal and calcareous nanofossil assemblages present in the Qimugun Formation indicate the presence of biozones P4, P5, E1, E2, and NP9 to NP10, respectively, which allows locating the Paleocene-Eocene boundary in the middle part of the unit, coinciding with the negative $\delta^{13}\text{C}$ and $\delta^{18}\text{O}$ excursions (Cao et al., 2018; Jiang et al., in prep; Jiang et al., 2018).

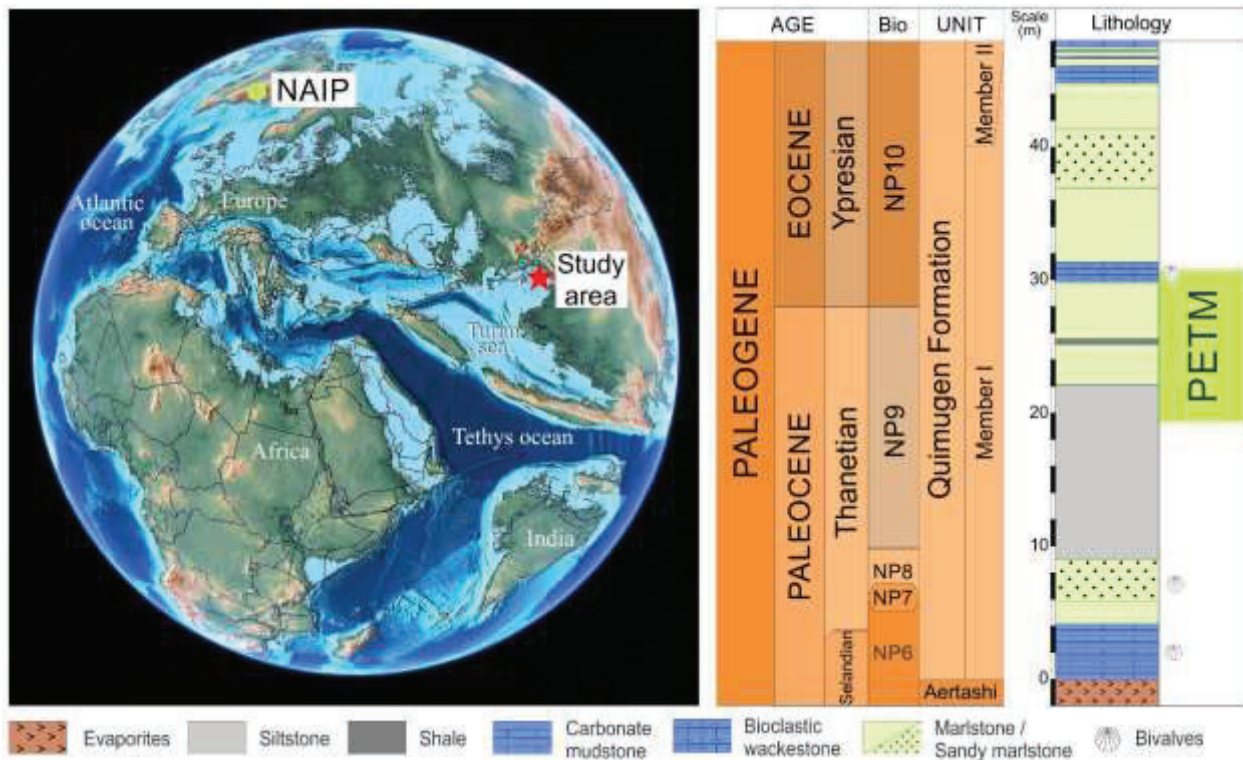


Figure 17: Paleogeography during the PETM (Scotese and Wright, 2018). Note the Tarim Basin (red star) and NAIP (light green circle). The lithology and age of the section confirm the presence of the PETM between 19.89 m to 30.5 m.

3. Methods

The samples chosen for BC analysis will aid in the reconstruction of the terrestrial conditions of the Tarim Basin during the late Paleocene and the PETM body. Unlike bulk

carbonates, which record marine signals, BC will provide signals on how terrestrial environments responded to the abrupt temperature change, which has yet to be understood at the Tarim Basin.

To begin, 480 rock samples were previously crushed into a powder with a SPEX zirconia ceramics ball mill at Montclair State University (MSU) for major and trace element analysis. Since each sample did not have enough powder to measure black carbon individually, gradients were created with two or three neighboring samples with similar colors (Table 4). The average depth of the sample gradients is also reported in Table 4. A total of 56 samples were measured to ~2 grams each in 15 mL Neoprene centrifuge tubes. The respective BC samples were chosen based on recent long-chain *n*-alkane data collected from the site (Jiang et al., in prep).

Table 4: Black carbon sample summary with composed KZGS samples, depth, and $\delta^{13}\text{C}$

<u>Average Depth (m)</u>	<u>BC Sample</u>	<u>KZGS Samples</u>	<u>$\delta^{13}\text{C}$ (‰)</u>
5.35	1	18, 19, 20	-24.39
5.61	2	21, 23	-24.36
7.97	3	32, 33, 34	-27.91
8.88	4	36, 37, 38	-23.57
9.17	5	39, 40, 41	-24.64
9.91	6	47, 48, 49	-20.32
10.37	7	52, 53, 54	-23.30
10.65	8	55, 56, 57	-23.88
10.97	9	59, 60	-23.13
11.25	10	62, 63	
11.43	11	64, 65	-24.13
11.61	12	66, 67	-24.28
11.98	13	70, 71	-23.48
12.69	14	78, 79	
13.72	15	87, 88	
14.08	16	90, 91	
14.43	17	93, 94	
14.67	18	95, 96	
14.90	19	97, 98	

15.91	20	105, 106, 107	
16.44	21	110, 111	
16.92	22	114, 115	-23.38
17.69	23	120, 121, 122	-24.41
18.04	24	123, 124, 125	
18.51	25	127, 128, 129	
18.81	26	130, 131	
19.26	27	134, 135	
20.25	28	141, 142	
20.75	29	144, 145, 146	
21.46	30	149, 150, 151	
21.93	31	153, 154, 155	
22.55	32	158, 159	
23.17	33	162, 163, 164	-25.42
23.59	34	165, 166, 167	-26.97
24.49	35	172, 173	-24.79
24.91	36	175, 176	-26.70
25.25	37	177, 179	-27.44
25.76	38	180, 182, 183	-26.80
26.17	39	184, 186	-25.54
26.57	40	189, 191	-27.19
26.99	41	194, 195, 197	-29.84
27.50	42	201, 203	-27.37
27.70	43	204, 205	
27.93	44	207, 208	
28.67	45	216, 217, 218	
29.02	46	221, 222	
29.41	47	226, 227	
29.79	48	231, 232	
30.08	49	234, 235, 236	
30.52	50	239, 240	
31.60	51	250, 251	
36.69	52	298, 299	
37.02	53	302, 303	
37.90	54	313, 314	
40.95	55	360, 361	
41.28	56	381, 382	

BC extraction follows the procedure described in Zhu et al. (2019) (details are shown in Fig. 18). First, each sample is treated with 10 mL of 6M HCl at 60°C in a Fisherbrand Isotemp general purpose water bath. Silicates are discarded with 10 mL of 22M HF + 6M HCl (2:1 ratio) for 20 hours at 60°C. The final carbonate removal is conducted with 6M HCl for 20 hours at 60°C. After each acid treatment, samples are centrifuged for 10 minutes at 5,000 rpm, decanted, and rinsed 3-5 times with 18.2Ω milliQ water.

When the acid digestion is completed, samples are chemically oxidized with 0.5M $K_2Cr_2O_7$ / 2M H_2SO_4 (potassium dichromate/ sulfuric acid) at 55°C to isolate BC for 12 days. Centrifuge tubes were fully submerged within the water bath to ensure heat was catalyzing the chemical reaction. As the water evaporates, it was replaced with 18.2Ω milliQ water to maintain a constant volume. When the oxidant discolored from its natural bright orange to a dark green, it was discarded and replaced with preheated potassium dichromate solution. When the oxidation process was completed, samples were cooled to room temperature and centrifuged for 30 minutes at 5,000 rpm. Each was then decanted, rinsed 3-5 times to ensure the pH is neutral, and dried in aluminum weighing dishes in an oven for 48 hours at 60°C.

Following this, the samples were weighed to 14.0 ± 0.5 mg in a microbalance and tin containers for isotope analysis. The elemental analyzer isotope ratio mass spectrometer (EA-IRMS) at MSU recorded the changes in $\delta^{13}C$ of 25 samples in the late Paleocene and early PETM body. The compiled data were compared to the KZGS bulk carbonate record, in addition to long-chain *n*-alkanes from the site analyzed in another study (Jiang et al., in prep). Major and trace element data were collected from an inductively coupled plasma mass spectrometer (ICP-MS) at MSU to compare weathering and redox proxies to changes in $\delta^{13}C_{BC}$ (Jiang et al., in prep).

A total of 5 samples were analyzed with a scanning electron microscope (SEM) at MSU to confirm the presence of BC. Samples were chosen based on carbon to nitrogen (C/ N) ratios that were greater than 10, indicating terrestrial origin. Due to its carbon-based nature, the samples were coated in a gold-palladium alloy. Surface morphologies and x-ray energy dispersive spectrometry (EDS) explored crystalline structures and elemental mapping and distribution, respectively. In conjunction with the previously established ICP-MS data (Jiang et al., in prep), potential chemical proxies for wildfires were identified within the samples.

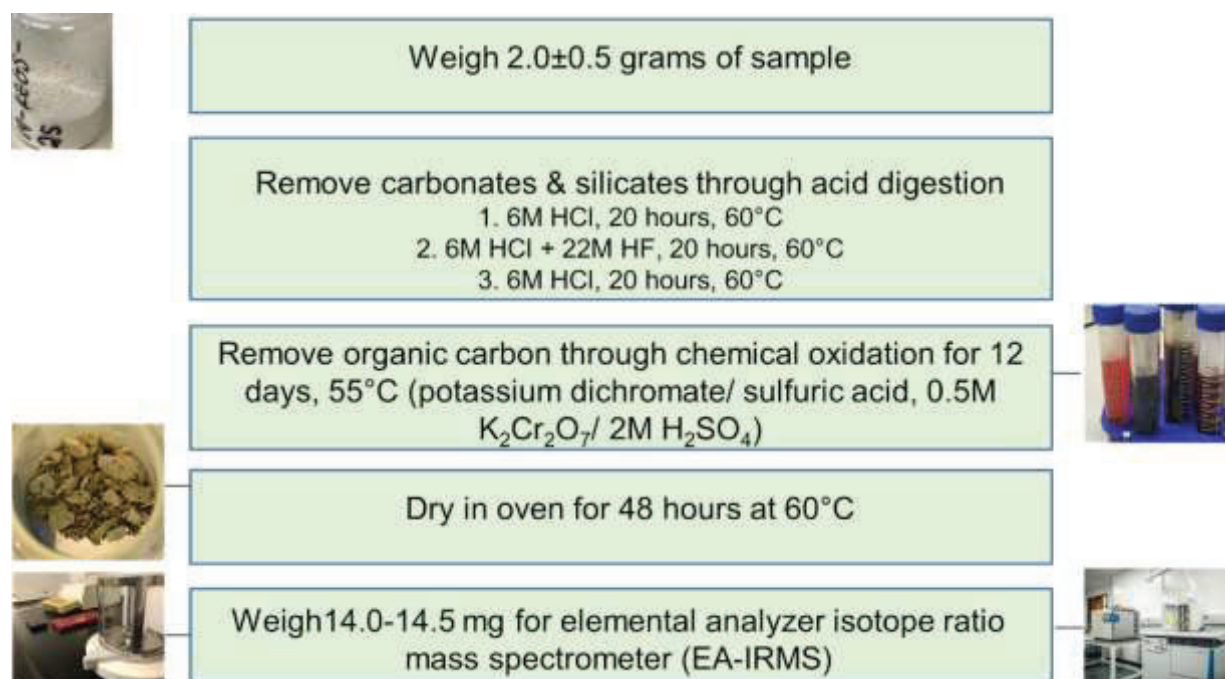


Figure 18: Black carbon extraction procedure following Zhu et al. (2019)

The mean annual precipitation (MAP) was calculated for the pre-PETM and the PETM body based on the methods described in Chen et al. (2020). The carbon isotope discrimination of photosynthesis (Δ_{leaf}) can be described as

$$\Delta_{leaf} = \frac{\delta^{13}C_{atm} - \delta^{13}C_{leaf}}{1 + \frac{\delta^{13}C_{leaf}}{1000}}$$

where $\delta^{13}\text{C}_{\text{atm}}$ and $\delta^{13}\text{C}_{\text{leaf}}$ are the averaged carbon isotopic ratios of atmospheric CO_2 and BC, respectively. A correction factor must be applied to each $\delta^{13}\text{C}$ to account for isotope fractionation. The $\epsilon_{\text{calcite-CO}_2(\text{g})}$, which is applied to $\delta^{13}\text{C}_{\text{atm}}$, is determined through

$$\epsilon_{\text{calcite-CO}_2(\text{g})} = 11.98 - 0.12 * \text{Temperature } (^\circ\text{C}).$$

Temperature for the pre-PETM, PETM, and post PETM were reconstructed through the site's oxygen isotope records ($\delta^{18}\text{O}$). The ϵ_{BC} enrichment factor is equal to 1.5‰ and applied to $\delta^{13}\text{C}_{\text{leaf}}$. MAP is then quantified through the following equation:

$$\Delta_{\text{leaf}} = 5.37(\pm 0.30) * \log(\text{MAP}) + 5.06(\pm 1.00)$$

4. Results

Figure 19 depicts the $\delta^{13}\text{C}$ of bulk carbonates and BC from the KZGS section. While both differ in their isotope values, they follow the same trend with values becoming more negative during the PETM. However, the BC record shows more depleted $\delta^{13}\text{C}$ values compared to the bulk carbonates. The most common $\delta^{13}\text{C}_{\text{BC}}$ values are between -24‰ to -23‰ (Fig. 20), likely because most of the results are sampled before the PETM or at the beginning of the event, before much change can be recorded. These values were further divided into time periods, which concluded that the average $\delta^{13}\text{C}$ were -24‰ and -27‰ for the pre-PETM and PETM, respectively (Fig. 21). The isotopic values from the KZGS section align with the $\delta^{13}\text{C}$ of Bass River, New Jersey, where the average $\delta^{13}\text{C}_{\text{BC}} = -23.2\text{‰}$ before the PETM and $\delta^{13}\text{C}_{\text{BC}} = -26.7\text{‰}$ during the PETM body (Moore and Kurtz, 2008).

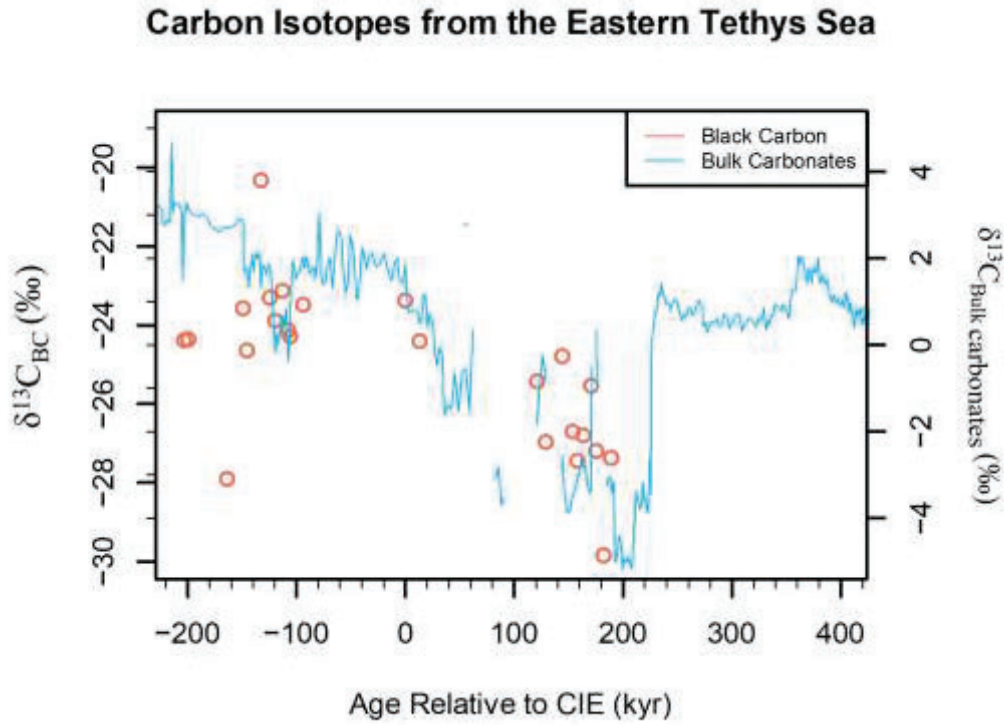


Figure 19: $\delta^{13}\text{C}$ of black carbon (red circles) and bulk carbonates (blue lines). Time zero represents the start of the CIE while negative time portrays the pre-PETM, and positive values represent time after the start of the CIE.

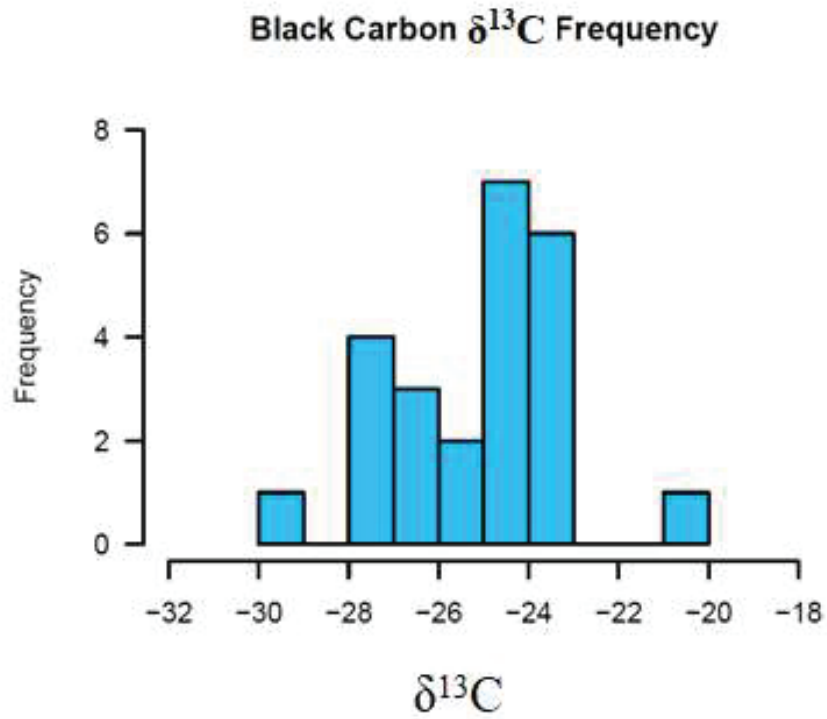


Figure 20: Frequency distribution of $\delta^{13}\text{C}_{\text{BC}}$. The results show that -23‰ and -24‰ are the most repeated values.

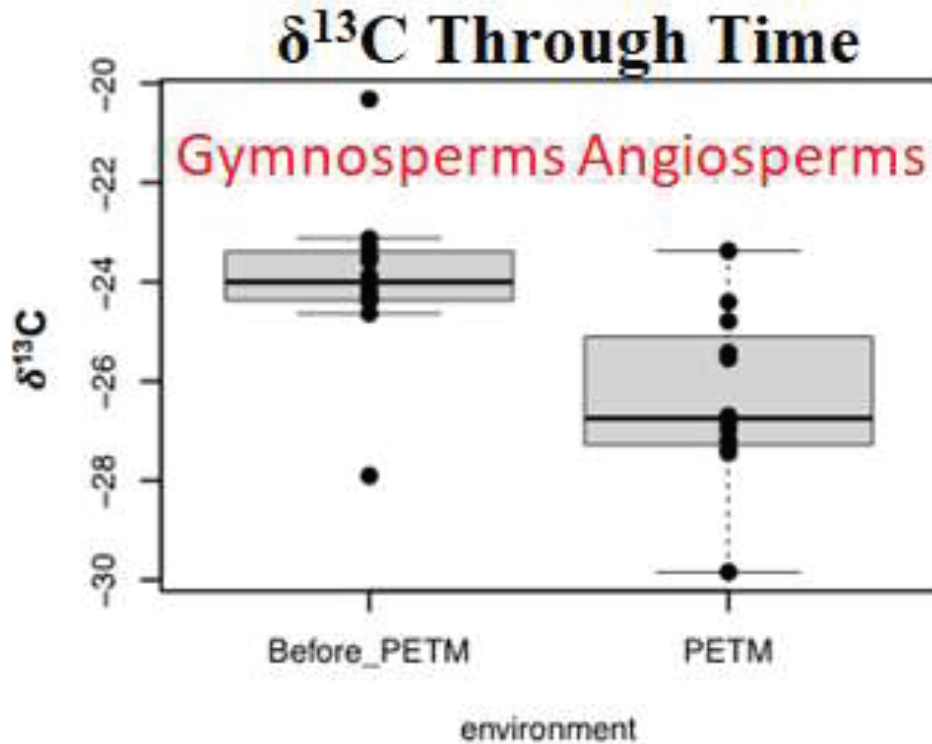


Figure 21: The distribution of the average $\delta^{13}\text{C}_{\text{BC}}$ between before and during the PETM.

The solid black line represents the mean of each dataset.

Averaged $\delta^{18}\text{O}$ determined that the temperature was 29.8°C and 44.6°C for the pre-PETM and PETM, respectively. Higher temperatures lead to a more active hydrological cycle in the eastern Tethys and delivered more precipitation to the region. This contributed to an increase in Δ_{leaf} values due to increased stomatal conductance and decreased water use efficiency (Chen et al., 2020). As such, the Δ_{leaf} values were determined to be 21.6‰ (pre-PETM) and 23.1‰ (PETM) with MAP increasing from 1,179 mm to 2,280 mm. As such, we determine that the eastern Tethys was an additional location that experienced extreme seasonal precipitation followed by dry seasons (Carmichael et al., 2017; Carmichael et al., 2018).

The wet and dry seasons are reflective in the C/N ratios during the PETM interval (Fig. 22). During rainy seasons, more terrestrial material, like BC and soil, are washed into the eastern Tethys, as highlighted by $C/N > 10$. However, during the dry seasons, $C/N < 10$, indicating organic matter originates from the marine environment.

Long-chain *n*-alkane (*n*-C₂₇, *n*-C₂₉, *n*-C₃₁) data from the KZGS section additionally show similar trends in $\delta^{13}C$ (Jiang et al., in prep) to $\delta^{13}C_{BC}$. Against the C/N ratios, the $\delta^{13}C$ of all substrates become more negative when C/N ratios > 10 , which further corresponds to changes in lithology (Fig. 22). Potassium oxide (K₂O) abundance additionally follows the trends in C/N ratios, supporting the influx of terrestrial material during the extreme, wet seasons.

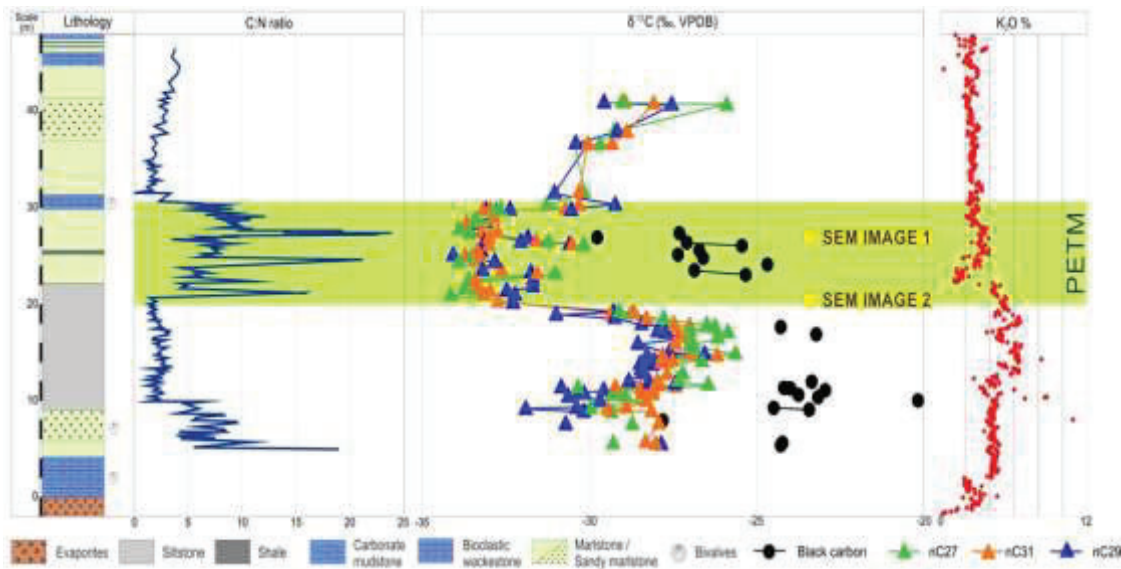


Figure 22: C/N ratios are denoted with blue curve. Note that when $C/N > 10$, the organic matter is believed to have terrestrial origin. $\delta^{13}C$ of black carbon (black circles) and long-chain *n*-alkanes (*n*-C₂₇, *n*-C₂₉, and *n*-C₃₁), shown in green, blue, and orange, respectively, borrowed from Jiang et al. (in prep). The presence of black carbon is noted with the yellow circles, which have only been found during the PETM thus far. The K₂O% is highlighted

as the red curve, which is borrowed from Jiang et al. (in prep). The dry and wet seasons can be observed with the various cyclic patterns in increasing and decreasing values in each of the curves.

Although samples 32, 34, and 36 were also investigated, SEM analysis could only confirm the presence of BC in samples 29 and 41, which contain high terrestrial input. The $K_2Cr_2O_7/2M H_2SO_4$ in samples 32, 34, and 36 changed color from bright orange to dark green 2-3 times during the BC extraction procedure, indicating that BC should be present in the sample despite the low C/N ratios; therefore, BC could either be in a region that was not investigated or too small for the SEM to detect. The EDS analysis indicates that silica, potassium, sulfur, and fluorine, are present within the samples, in addition to other trace metals (Fig. 23-24).

Image 1

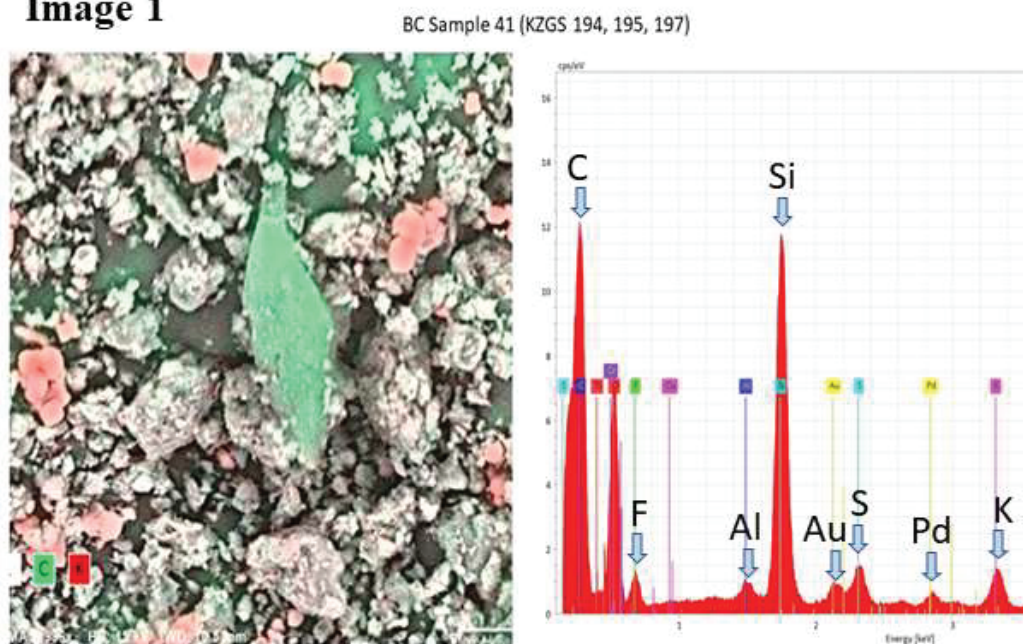


Figure 23: SEM image of black carbon from 41 (KZGS 194, 195, 197). Elemental mapping highlights a carbon-based particle in green (left). The EDS analysis shows all the elements present in the entire region (right).

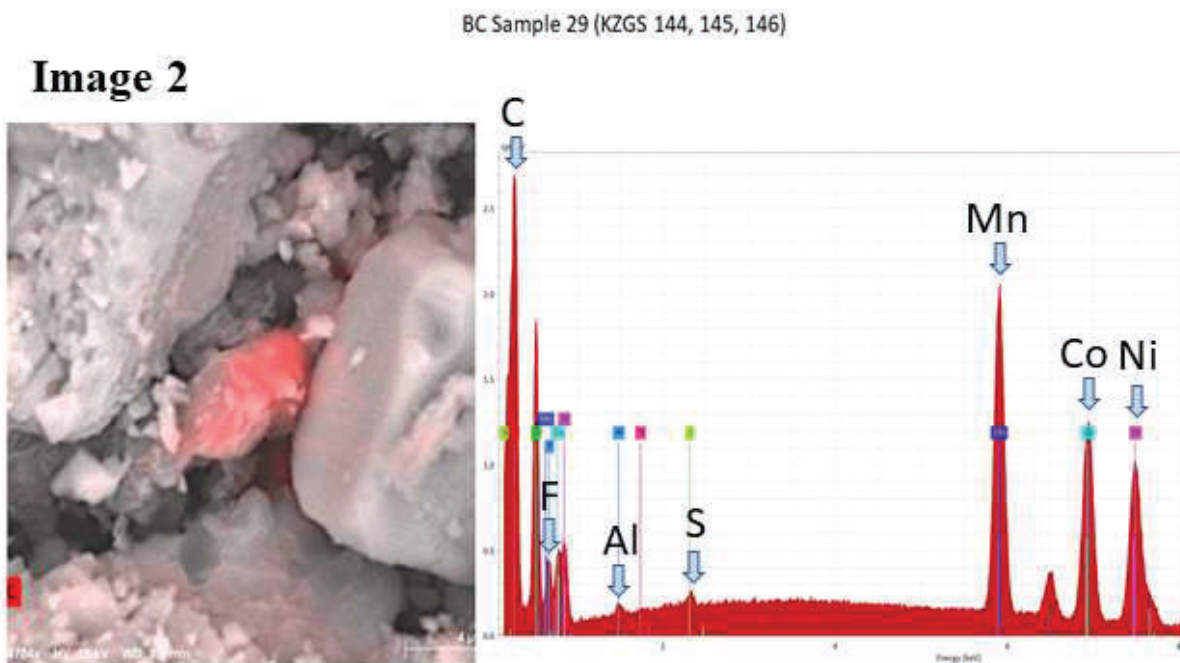


Figure 24: SEM image of black carbon from sample 29 (KZGS 144, 145, 146). Elemental mapping highlights a carbon-based particle in red (left) while the EDS analysis depicts the elements present in the entire region (right).

5. Discussion

In comparison to bulk carbonates, which records signals from the ocean, BC only originates from land plants, providing a clear explanation of how the eastern Tethys terrestrial ecosystems responded to the PETM. In the late Paleocene, the eastern Tethys was a semi-arid environment, as indicated by the presence of gypsum and evaporites at the base of the stratigraphic column (Cao et al., 2018; Jiang et al., in prep). The drier conditions are reflective in high $\delta^{13}\text{C}$ values, possibly indicating gymnosperms were present in the region. It has been found that gymnosperms favor drier conditions and contain $\delta^{13}\text{C}$ ranging from -28‰ to -16‰, with an average $\delta^{13}\text{C} = -23\text{‰}$ (Li et al., 2021; Sheldon et al., 2020). Angiosperms, however, favor wetter and warmer conditions and have a smaller range of $\delta^{13}\text{C}$ from -28‰ to -20‰, with an average

$\delta^{13}\text{C} = -24.5\text{‰}$ (Augusto et al., 2015; Li et al., 2021; Pedentchouk et al., 2008). More precipitation can also influence the $\delta^{13}\text{C}$, leading to more negative values due to increased stomatal conductance and decreased water use efficiency (Chen et al., 2020; Diefendorf et al., 2010; Rush et al., 2021). In response, to increased precipitation the Δ_{leaf} values will rise.

As such, the shift in $\delta^{13}\text{C}$ values is interpreted as warmer temperatures and increased precipitation contributing to a vegetation shift of gymnosperms to angiosperms. Specifically, the migration or failure of adaptation of gymnosperms and the invasion of heat tolerant angiosperms could have been the result of new environmental conditions. This would be unsurprising since gymnosperms are absent in most sites during the PETM and angiosperms expanded and diversified (Jaramillo et al., 2010; McInerney and Wing, 2011). It is recommended that palynology analysis is conducted at the KZGS section to confirm this. The data also indicates that the plants in the eastern Tethys were of C_3 origin, which is to be expected since C_4 plants did not yet exist (Westhoff and Gowik, 2010).

The SEM imaging and elemental mapping confirm the presence of carbon-based substances. Following the acid digestion and chemical oxidation, any carbon remaining is believed to be BC (Zhu et al., 2019). The procedure developed by Zhu et al. (2019) has the highest success rate of extracting BC in sedimentary rocks with Type I maturity, yet the KZGS samples are of Type III (Jiang et al., in prep) (Fig. S4). This could potentially limit the success rate of BC extraction, but chemical oxidation is recommended until a specific procedure can be developed specifically for Type III maturity samples. However, the presence of BC in samples with rocks of terrestrial-origin C/N ratios suggests that regional wildfires could have occurred, and the increased precipitation likely transported the BC through runoff (Collinson et al., 2007).

The extreme, seasonal precipitation during the PETM could have additionally led to accelerated growth of biomass during the wet seasons, providing more fuel to burn during the dry seasons (Lu et al., 2020). Higher concentrations of $p\text{CO}_2$ lead to lightning-induced wildfires during the PETM, despite increased moisture transport (Denis et al., 2017; Fung et al., 2019). Terrestrial runoff and increased soil erosion have additionally been recognized after fire events, possibly delivering some of the nutrients observed in the EDS analysis to the eastern Tethys (Collinson et al., 2007; Synnott et al., 2021). Specifically, the sulfur peaks (Figs. 23-24) could originate from sulfur dioxide emissions from wildfires or the NAIP degassing (Sun et al., 2017). Although likely not originating from wildfires, trace amounts of fluorine have been recorded from volcanic eruptions, which support the NAIP degassing (Punekar et al., 2014). However, fluorine signals could also be remnant of the HF acid treatment. In conjunction with rock weathering, plant combustion and soil erosion could explain a partial component of the potassium increases from the ICP-MS data and the EDS analysis (Lu et al., 2020). The presence of marlstone, shale, and mudstone clastic (beginning ~21 m) are additional indicators of increased clay, terrestrial input, and soil erosion (Lu et al., 2020). The presence of increased illite abundance during the CIE in the Bashibulake section of the Tarim Basin further supports physical weathering from intense seasonal precipitation (Cao et al., 2018; Hollaar et al., 2021). Changes in lithology additionally reflect C/N ratio and $\delta^{13}\text{C}$ shifts, as a result of increased terrestrial input.

The transport of additional nutrients from increased precipitation and runoff to the eastern Tethys at the beginning of the PETM is suggested in SEM image 2. This sample shows a peak of nickel (Fig. 24), which is a common element in sedimentary deposits rich in organic matter and a proxy for increased paleo-productivity (Tribovillard, 2021; Tribovillard et al., 2006). ICP-MS

analysis shows periodic increases in the Ni/Al ratio, supporting episodic rises in the nutrient supply in the eastern Tethys (Jiang et al., in prep). The EDS analysis also shows signals of cobalt, which increases coincident in time with nickel (Jiang et al., in prep), but there is debate whether this is a reliable proxy for paleo-productivity (Tribovillard, 2021; Tribovillard et al., 2006), and as such, is not considered in this study for paleo-productivity. Although the sedimentary sequence of the studied section is generally poor in organic matter, as suggested by the light color of the sediments, the darker colored levels correspond to the segments where we detected BC. This suggests a higher organic matter content and periods of anoxia at the beginning of the PETM, which has been supported by higher V/Al and V/Cr ratios (Jiang et al., in prep). The event delivered more precipitation to the region, and the runoff washed terrestrial material and nutrients into the eastern Tethys, fueling eutrophication. However, the fluctuations in Ni/Al, V/Al, and V/Cr support episodic periods of anoxia during the extreme, wet season rather than constant anoxia like some modeling results show (Remmelzwaal et al., 2019). The drastic increases in the C/N ratio support this. Eutrophication resulted in anoxic bottom water conditions, likely contributing to the benthic foraminifera mass extinction (Cao et al., 2018; Remmelzwaal et al., 2019).

In many cases, nickel may not accurately reflect the amount of organic matter (OM) initially deposited. Losses associated with decomposition of OM before conditions conducive to sulfate-reduction occur or a low abundance of reactive iron limiting the amount of pyrite likely to form may result in nickel not being retained in the sediments. Paleo-environmental reconstructions involving the concentrations of this metal may provide underestimated values of paleo-productivity. To determine this, it is suggested that future studies determine the Fe/Al ratio, which allows us to know if these enrichment values can be “abnormally” low (Tribovillard,

2021). Furthermore, the presence of manganese in image 2 supports redox conditions (Tribovillard et al., 2006) (Fig. 24). Specifically, redox conditions are supported with Mn^* , which is defined as $\log[(Mn_{\text{sample}}/ Mn_{\text{shale}})/ (Fe_{\text{sample}}/ Fe_{\text{shale}})]$. Previous work has shown Mn^* remains negative during the PETM and swiftly becomes positive following the event (Jiang et al., in prep).

6. Conclusion

The carbon cycle perturbations and rapid global warming of the PETM was likely the result of the NAIP CO_2 degassing. Prior to the PETM, the eastern Tethys was a semi-arid environment that was likely prone to wildfires. The rapid warming from the PETM fueled an accelerated hydrological cycle, delivering more precipitation to the eastern Tethys and suppressing the occurrence of fires. These changes in climate likely shifted the vegetation from gymnosperms to angiosperms, as indicated by $\delta^{13}C_{BC}$. The $\delta^{13}C_{BC}$ matches trends observed in $\delta^{13}C_{n\text{-alkanes}}$ and $\delta^{13}C_{\text{carb}}$ from the study site, and the $\delta^{13}C_{BC}$ record from Bass River, New Jersey. The changes in $\delta^{13}C_{BC}$ additionally align with shifts in lithology, C/N ratios, and potassium concentrations. To confirm the shift in vegetation and terrestrial ecosystem responses, it is suggested that palynology analysis should be conducted at the KZGS section. The work done here can be applied to modern climate change to infer how vegetation will respond to increased wildfire occurrences as a result of anthropogenic climate change.

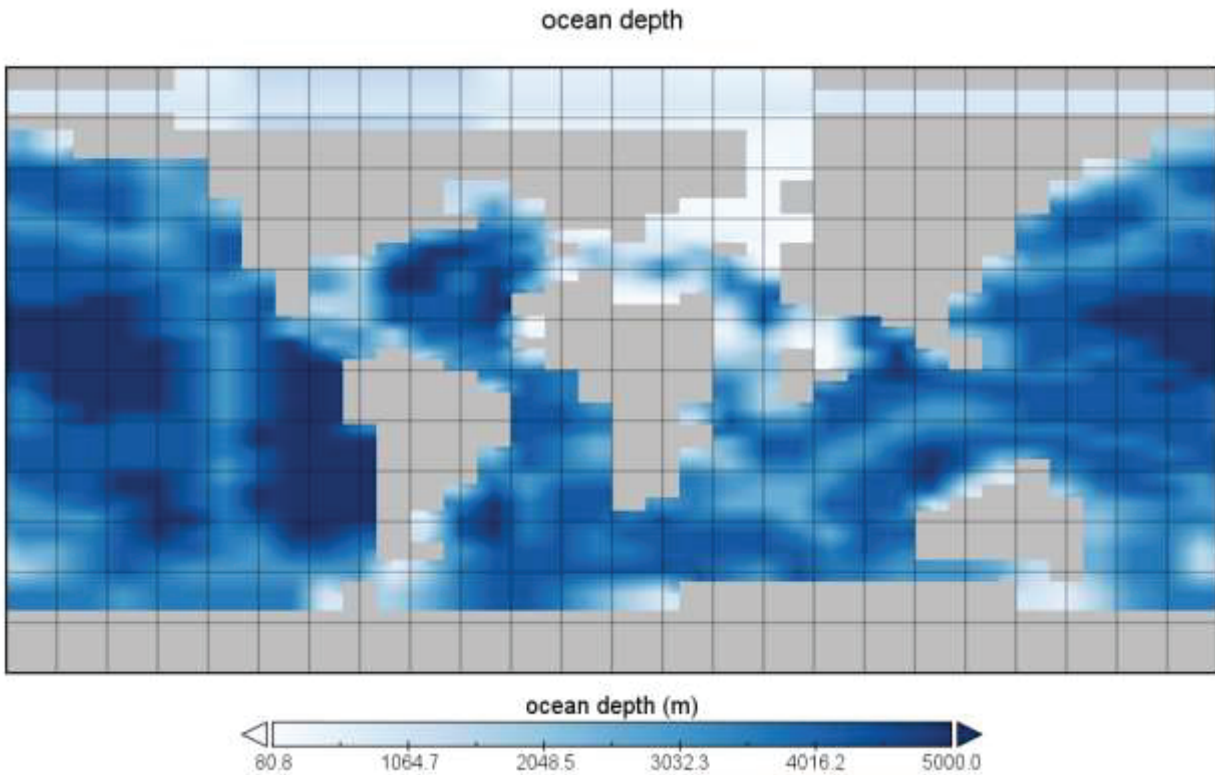
Supplemental Figures

Figure S1: The cGENIE representation of global bathymetry with an early Eocene continental configuration (55 Ma).

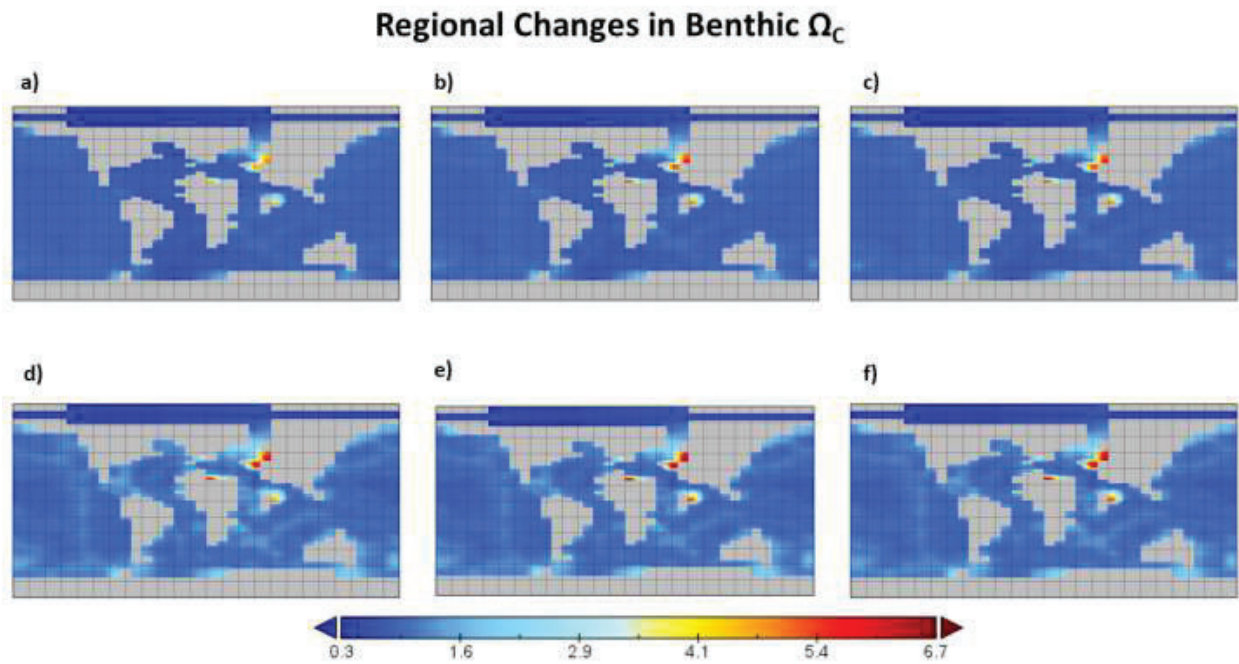


Figure S2: Regional changes in benthic Ω_C at the lowest point in concentration (45 kyr; top row) and the beginning of the recovery (90 kyr; bottom row). A) and D) low scenario; B) and E) medium scenario; C) and F) high scenario

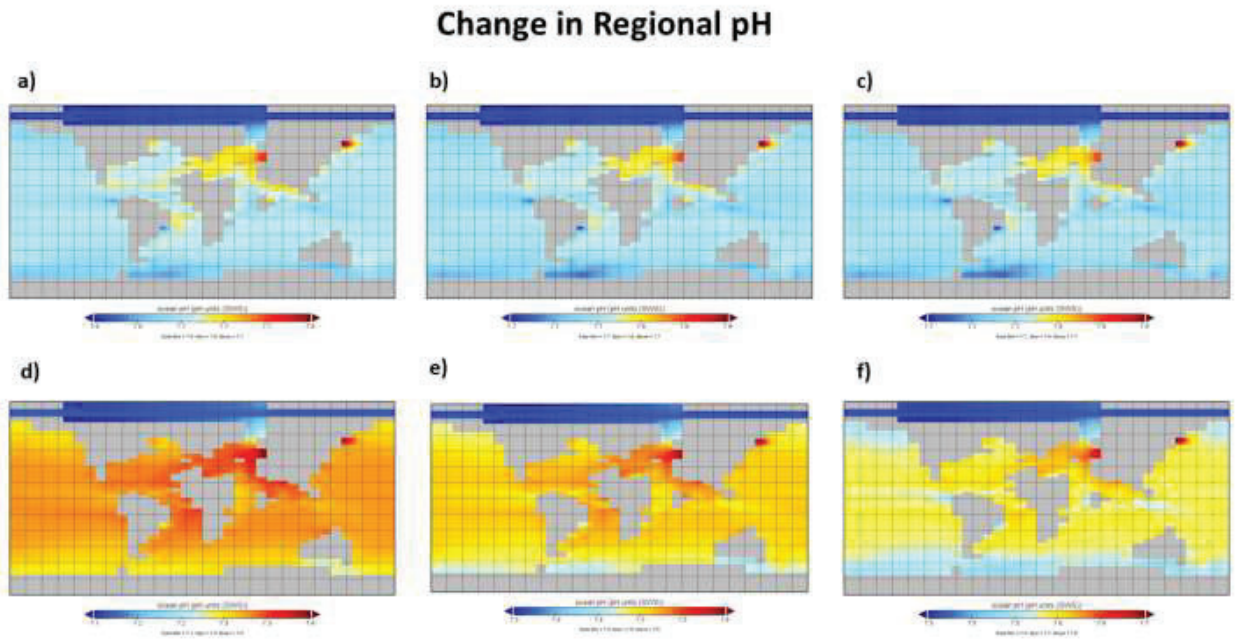


Figure S3: Regional changes in pH 100 years after the CIE (top row) and each experiment's lowest point in pH (bottom row) A) low scenario; B) medium scenario; C) high scenario; D) low scenario at 85 kyr; E) medium scenario at 80 kyr; F) high scenario at 75 kyr.

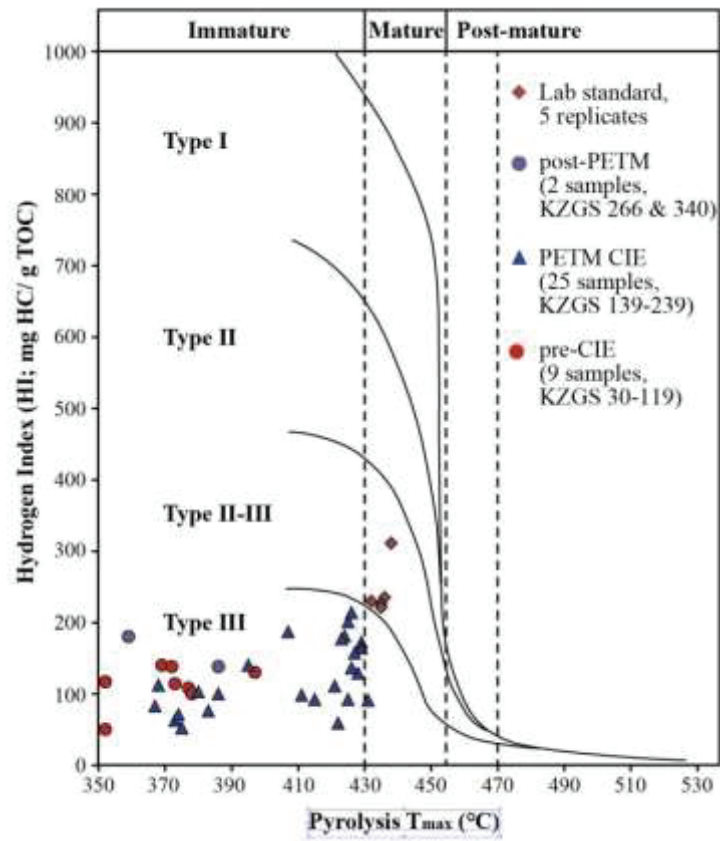


Figure S4: Thermal maturity of the KZGS samples fall mostly within Type III classification (Jiang et al., in prep).

References

- Abigail, R., Clyde, W.C., Fricke, H.C., Gingerich, P.D., Abels, H.A., 2017. Repetitive mammalian dwarfing during ancient greenhouse warming events. *Science Advances* 3, e1601430.
- Adloff, M., Greene, S.E., Parkinson, I.J., Naafs, B.D.A., Preston, W., Ridgwell, A., Lunt, D.J., Castro Jiménez, J.M., Monteiro, F.M., 2020. Unravelling the sources of carbon emissions at the onset of Oceanic Anoxic Event (OAE) 1a. *Earth and Planetary Science Letters* 530.
- Alegret, L., Arreguín-Rodríguez, G.J., Trasviña-Moreno, C.A., Thomas, E., 2021. Turnover and stability in the deep sea: Benthic foraminifera as tracers of Paleogene global change. *Global and Planetary Change* 196, 103372.
- Alegret, L., Ortiz, S., Orue-Etxebarria, X., Bernaola, G., Baceta, J.I., Monechi, S., Apellaniz, E., Pujalte, V., 2009. The Paleocene–Eocene thermal maximum: new data on microfossil turnover at the Zumaia section, Spain. *Palaios* 24, 318-328.
- Augusto, L., De Schrijver, A., Vesterdal, L., Smolander, A., Prescott, C., Ranger, J., 2015. Influences of evergreen gymnosperm and deciduous angiosperm tree species on the functioning of temperate and boreal forests. *Biological Reviews* 90, 444-466.
- Babila, T.L., Penman, D.E., Hönisch, B., Kelly, D.C., Bralower, T.J., Rosenthal, Y., Zachos, J.C., 2018. Capturing the global signature of surface ocean acidification during the Palaeocene-Eocene Thermal Maximum. *Philos Trans A Math Phys Eng Sci* 376, 20170072.
- Babila, T.L., Penman, D.E., Standish, C.D., Doubrava, M., Bralower, T.J., Robinson, M.M., Self-Trail, J.M., Speijer, R.P., Stassen, P., Foster, G.L., 2022. Surface ocean warming and acidification driven by rapid carbon release precedes Paleocene-Eocene Thermal Maximum. *Science Advances* 8, eabg1025.
- Baker, S.J., 2022. Fossil evidence that increased wildfire activity occurs in tandem with periods of global warming in Earth's past. *Earth-Science Reviews* 224, 103871.
- Bowen, G.J., Maibauer, B.J., Kraus, M.J., Röhl, U., Westerhold, T., Steimke, A., Gingerich, P.D., Wing, S.L., Clyde, W.C., 2015. Two massive, rapid releases of carbon during the onset of the Palaeocene–Eocene thermal maximum. *Nature Geoscience* 8, 44-47.
- Bowen, G.J., Zachos, J.C., 2010. Rapid carbon sequestration at the termination of the Palaeocene–Eocene Thermal Maximum. *Nature Geoscience* 3, 866-869.
- Breitburg, D., Levin, L.A., Oschlies, A., Grégoire, M., Chavez, F.P., Conley, D.J., Garçon, V., Gilbert, D., Gutiérrez, D., Isensee, K., 2018. Declining oxygen in the global ocean and coastal waters. *Science* 359, eaam7240.
- Cao, W., Xi, D., Melinte-Dobrinescu, M.C., Jiang, T., Wise, S.W., Wan, X., 2018. Calcareous nannofossil changes linked to climate deterioration during the Paleocene–Eocene thermal maximum in Tarim Basin, NW China. *Geoscience Frontiers* 9, 1465-1478.
- Carmichael, M.J., Inglis, G.N., Badger, M.P., Naafs, B.D.A., Behrooz, L., Remmelzwaal, S., Monteiro, F.M., Rohrssen, M., Farnsworth, A., Buss, H.L., 2017. Hydrological and associated biogeochemical consequences of rapid global warming during the Paleocene-Eocene Thermal Maximum. *Global and Planetary Change* 157, 114-138.
- Carmichael, M.J., Pancost, R.D., Lunt, D.J., 2018. Changes in the occurrence of extreme precipitation events at the Paleocene–Eocene thermal maximum. *Earth and Planetary Science Letters* 501, 24-36.
- Charles, A.J., Condon, D.J., Harding, I.C., Pälike, H., Marshall, J.E., Cui, Y., Kump, L., Croudace, I.W., 2011. Constraints on the numerical age of the Paleocene-Eocene boundary. *Geochemistry, Geophysics, Geosystems* 12.

- Chen, Z., Dong, X., Wang, X., Tang, Z., Yang, S., Zhu, M., Ding, Z., 2020. Spatial change of precipitation in response to the Paleocene-Eocene thermal Maximum warming in China. *Global and Planetary Change* 194, 103313.
- Cheng, L., Normandeau, C., Bowden, R., Doucett, R., Gallagher, B., Gillikin, D.P., Kumamoto, Y., McKay, J.L., Middlestead, P., Ninnemann, U., Nothaft, D., Dubinina, E.O., Quay, P., Reverdin, G., Shirai, K., Mørkved, P.T., Theiling, B.P., van Geldern, R., Wallace, D.W.R., 2019. An international intercomparison of stable carbon isotope composition measurements of dissolved inorganic carbon in seawater. *Limnology and Oceanography: Methods* 17, 200-209.
- Clarkson, M.O., Lenton, T.M., Andersen, M.B., Bagard, M.-L., Dickson, A.J., Vance, D., 2021. Upper limits on the extent of seafloor anoxia during the PETM from uranium isotopes. *Nature communications* 12, 1-9.
- Collinson, M.E., Steart, D., Scott, A., Glasspool, I., Hooker, J., 2007. Episodic fire, runoff and deposition at the Palaeocene–Eocene boundary. *Journal of the Geological Society* 164, 87-97.
- Cui, Y., Kump, L.R., Ridgwell, A.J., Charles, A.J., Junium, C.K., Diefendorf, A.F., Freeman, K.H., Urban, N.M., Harding, I.C., 2011. Slow release of fossil carbon during the Palaeocene–Eocene Thermal Maximum. *Nature Geoscience* 4, 481-485.
- Cui, Y., Schubert, B.A., 2018. Towards determination of the source and magnitude of atmospheric pCO₂ change across the early Paleogene hyperthermals. *Global and Planetary Change* 170, 120-125.
- DeConto, R.M., Galeotti, S., Pagani, M., Tracy, D., Schaefer, K., Zhang, T., Pollard, D., Beerling, D.J., 2012. Past extreme warming events linked to massive carbon release from thawing permafrost. *Nature* 484, 87-91.
- Denis, E.H., Pedentchouk, N., Schouten, S., Pagani, M., Freeman, K.H., 2017. Fire and ecosystem change in the Arctic across the Paleocene–Eocene Thermal Maximum. *Earth and Planetary Science Letters* 467, 149-156.
- Dickens, G.R., Castillo, M.M., Walker, J.C.G., 1997. A blast of gas in the latest Paleocene: Simulating first-order effects of massive dissociation of oceanic methane hydrate. *Geology* 25, 259-262.
- Diefendorf, A.F., Mueller, K.E., Wing, S.L., Koch, P.L., Freeman, K.H., 2010. Global patterns in leaf 13C discrimination and implications for studies of past and future climate. *Proceedings of the National Academy of Sciences* 107, 5738-5743.
- Dunkley Jones, T., Lunt, D.J., Schmidt, D.N., Ridgwell, A., Sluijs, A., Valdes, P.J., Maslin, M., 2013. Climate model and proxy data constraints on ocean warming across the Paleocene–Eocene Thermal Maximum. *Earth-Science Reviews* 125, 123-145.
- Dunkley Jones, T., Ridgwell, A., Lunt, D., Maslin, M., Schmidt, D., Valdes, P., 2010. A Palaeogene perspective on climate sensitivity and methane hydrate instability. *Philosophical Transactions of the Royal Society A: Mathematical, Physical and Engineering Sciences* 368, 2395-2415.
- Frieling, J., Gebhardt, H., Huber, M., Adekeye, O.A., Akande, S.O., Reichart, G.J., Middleburg, J.J., Schouten, S., Sluijs, A., 2017. Extreme warmth and heat-stressed plankton in the tropics during the Paleocene-Eocene Thermal Maximum. *Science Advances* 3.
- Frieling, J., Peterse, F., Lunt, D., Bohaty, S., Sinninghe Damsté, J., Reichart, G.J., Sluijs, A., 2019. Widespread warming before and elevated barium burial during the Paleocene-Eocene Thermal Maximum: Evidence for methane hydrate release? *Paleoceanography and paleoclimatology* 34, 546-566.
- Frieling, J., Svensen, H.H., Planke, S., Cramwinckel, M.J., Selnes, H., Sluijs, A., 2016. Thermogenic methane release as a cause for the long duration of the PETM. *Proceedings of the National Academy of Sciences* 113, 12059-12064.
- Fung, M., Schaller, M., Hoff, C., Katz, M., Wright, J., 2019. Widespread and intense wildfires at the Paleocene-Eocene boundary. *Geochemical Perspectives Letters*.

- Garel, S., Schnyder, J., Jacob, J., Dupuis, C., Boussafir, M., Le Milbeau, C., Storme, J.-Y., Iakovleva, A.I., Yans, J., Baudin, F., Fléhoc, C., Quesnel, F., 2013. Paleohydrological and paleoenvironmental changes recorded in terrestrial sediments of the Paleocene–Eocene boundary (Normandy, France). *Palaeogeography, Palaeoclimatology, Palaeoecology* 376, 184-199.
- Gibbs, S.J., Bralower, T.J., Bown, P.R., Zachos, J.C., Bybell, L.M., 2006. Shelf and open-ocean calcareous phytoplankton assemblages across the Paleocene-Eocene Thermal Maximum: Implications for global productivity gradients. *Geology* 34, 233-236.
- Griffith, E.M., Fantle, M.S., Eisenhauer, A., Paytan, A., Bullen, T.D., 2015. Effects of ocean acidification on the marine calcium isotope record at the Paleocene–Eocene Thermal Maximum. *Earth and Planetary Science Letters* 419, 81-92.
- Gutjahr, M., Ridgwell, A., Sexton, P.F., Anagnostou, E., Pearson, P.N., Pälike, H., Norris, R.D., Thomas, E., Foster, G.L., 2017. Very large release of mostly volcanic carbon during the Palaeocene–Eocene Thermal Maximum. *Nature* 548, 573-577.
- Handley, L., Crouch, E.M., Pancost, R.D., 2011. A New Zealand record of sea level rise and environmental change during the Paleocene–Eocene Thermal Maximum. *Palaeogeography, Palaeoclimatology, Palaeoecology* 305, 185-200.
- Hollaar, T.P., Baker, S.J., Hesselbo, S.P., Deconinck, J.-F., Mander, L., Ruhl, M., Belcher, C.M., 2021. Wildfire activity enhanced during phases of maximum orbital eccentricity and precessional forcing in the Early Jurassic. *Communications Earth & Environment* 2, 247.
- Hurdeman, E., Frieling, J., Reichgelt, T., Bijl, P., Bohaty, S., Holdgate, G., Gallagher, S., Peterse, F., Greenwood, D., Pross, J., 2021. Rapid expansion of meso-megathermal rain forests into the southern high latitudes at the onset of the Paleocene-Eocene Thermal Maximum. *Geology* 49, 40-44.
- Inglis, G.N., Rohrsen, M., Kennedy, E.M., Crouch, E.M., Raine, J.I., Strogen, D.P., Naafs, B.D.A., Collinson, M.E., Pancost, R.D., 2020. Terrestrial methane cycle perturbations during the onset of the Paleocene-Eocene Thermal Maximum. *Geology*.
- Jaramillo, C., Cárdenas, A., 2013. Global Warming and Neotropical Rainforests: A Historical Perspective. *Annual Review of Earth and Planetary Sciences* 41, 741-766.
- Jaramillo, C., Ochoa, D., Contreras, L., Pagani, M., Carvajal-Ortiz, H., Pratt, L.M., Krishnan, S., Cardona, A., Romero, M., Quiroz, L., 2010. Effects of rapid global warming at the Paleocene-Eocene boundary on neotropical vegetation. *Science* 330, 957-961.
- Jiang, S., Cui, Y., Wang, Y., De Palma, M., Naafs, B.D.A., Jiang, K., Wu, H., Bralower, T.J., Zachos, J., in prep. Volcanism triggered carbon emission and feedbacks across the PETM *Nature Geoscience*.
- Jiang, T., Wan, X., Aitchison, J.C., Xi, D., Cao, W., 2018. Foraminiferal response to the PETM recorded in the SW Tarim Basin, central Asia. *Palaeogeography, Palaeoclimatology, Palaeoecology* 506, 217-225.
- Jones, M.T., Percival, L.M.E., Stokke, E.W., Frieling, J., Mather, T.A., Riber, L., Schubert, B.A., Schultz, B., Tegner, C., Planke, S., Svensen, H.H., 2019a. Mercury anomalies across the Palaeocene–Eocene Thermal Maximum. *Climate of the Past* 15, 217-236.
- Jones, S.M., Hoggett, M., Greene, S.E., Dunkley Jones, T., 2019b. Large Igneous Province thermogenic greenhouse gas flux could have initiated Paleocene-Eocene Thermal Maximum climate change. *Nature Communications* 10, 5547.
- Kapetanaki, N., Krasakopoulou, E., Stathopoulou, E., Dassenakis, M., Scoullou, M., 2020. Severe coastal hypoxia interchange with ocean acidification: An experimental perturbation study on carbon and nutrient biogeochemistry. *Journal of Marine Science and Engineering* 8, 462.

- Keller, G., Mateo, P., Punekar, J., Khozyem, H., Gertsch, B., Spangenberg, J., Bitchong, A.M., Adatte, T., 2018. Environmental changes during the Cretaceous-Paleogene mass extinction and Paleocene-Eocene Thermal Maximum: Implications for the Anthropocene. *Gondwana Research* 56, 69-89.
- Kelly, D.C., Zachos, J.C., Bralower, T.J., Schellenberg, S.A., 2005. Enhanced terrestrial weathering/runoff and surface ocean carbonate production during the recovery stages of the Paleocene-Eocene thermal maximum. *Paleoceanography* 20.
- Kender, S., Stephenson, M.H., Riding, J.B., Leng, M.J., Knox, R.W.O.B., Peck, V.L., Kendrick, C.P., Ellis, M.A., Vane, C.H., Jamieson, R., 2012. Marine and terrestrial environmental changes in NW Europe preceding carbon release at the Paleocene–Eocene transition. *Earth and Planetary Science Letters* 353-354, 108-120.
- Kirtland Turner, S., Ridgwell, A., 2016. Development of a novel empirical framework for interpreting geological carbon isotope excursions, with implications for the rate of carbon injection across the PETM. *Earth and Planetary Science Letters* 435, 1-13.
- Kraus, M.J., Riggins, S., 2007. Transient drying during the Paleocene–Eocene Thermal Maximum (PETM): analysis of paleosols in the Bighorn Basin, Wyoming. *Palaeogeography, Palaeoclimatology, Palaeoecology* 245, 444-461.
- Kump, L.R., Bralower, T.J., Ridgwell, A., 2009. Ocean acidification in deep time. *Oceanography* 22, 94-107.
- Kurtz, A.C., Kump, L.R., Arthur, M.A., Zachos, J.C., Paytan, A., 2003. Early Cenozoic decoupling of the global carbon and sulfur cycles. *Paleoceanography* 18.
- Li, J., Hu, X., Zachos, J.C., Garzanti, E., BouDagher-Fadel, M., 2020. Sea level, biotic and carbon-isotope response to the Paleocene–Eocene thermal maximum in Tibetan Himalayan platform carbonates. *Global and Planetary Change* 194, 103316.
- Li, X., Chen, G., Qin, W., Wang, X., Liu, H., Wang, P., 2021. Differences in responses of tree-ring $\delta^{13}\text{C}$ in angiosperms and gymnosperms to climate change on a global scale. *Forest Ecology and Management* 492, 119247.
- Lourens, L.J., Sluijs, A., Kroon, D., Zachos, J.C., Thomas, E., Röhl, U., Bowles, J., Raffi, I., 2005. Astronomical pacing of late Palaeocene to early Eocene global warming events. *Nature* 435, 1083-1087.
- Lu, J., Zhang, P., Yang, M., Shao, L., Hilton, J., 2020. Continental records of organic carbon isotopic composition ($\delta^{13}\text{C}_{\text{org}}$), weathering, paleoclimate and wildfire linked to the End-Permian Mass Extinction. *Chemical Geology* 558, 119764.
- McInerney, F.A., Wing, S.L., 2011. The Paleocene-Eocene Thermal Maximum: A Perturbation of Carbon Cycle, Climate, and Biosphere with Implications for the Future. *Annual Review of Earth and Planetary Sciences* 39, 489-516.
- Meissner, K.J., Bralower, T.J., Alexander, K., Jones, T.D., Sijp, W., Ward, M., 2014. The Paleocene-Eocene Thermal Maximum: How much carbon is enough? *Paleoceanography* 29, 946-963.
- Moore, E.A., Kurtz, A.C., 2008. Black carbon in Paleocene–Eocene boundary sediments: A test of biomass combustion as the PETM trigger. *Palaeogeography, Palaeoclimatology, Palaeoecology* 267, 147-152.
- Nagy, J., Jargvoll, D., Dypvik, H., Jochmann, M., Riber, L., 2013. Environmental changes during the Paleocene–Eocene Thermal Maximum in Spitsbergen as reflected by benthic foraminifera. *Polar Research* 32, 19737.
- Pagani, M., Pedentchouk, N., Huber, M., Sluijs, A., Schouten, S., Brinkhuis, H., Damsté, J.S.S., Dickens, G.R., 2006. Arctic hydrology during global warming at the Palaeocene/Eocene thermal maximum. *Nature* 442, 671-675.
- Panchuk, K., Ridgwell, A., Kump, L.R., 2008. Sedimentary response to Paleocene-Eocene Thermal Maximum carbon release: A model-data comparison. *Geology* 36, 315-318.

- Pedentchouk, N., Sumner, W., Tipple, B., Pagani, M., 2008. $\delta^{13}\text{C}$ and δD compositions of n-alkanes from modern angiosperms and conifers: An experimental set up in central Washington State, USA. *Organic Geochemistry* 39, 1066-1071.
- Penman, D.E., 2016. Silicate weathering and North Atlantic silica burial during the Paleocene-Eocene thermal maximum. *Geology* 44, 731-734.
- Penman, D.E., Hönisch, B., Zeebe, R.E., Thomas, E., Zachos, J.C., 2014. Rapid and sustained surface ocean acidification during the Paleocene-Eocene Thermal Maximum. *Paleoceanography* 29, 357-369.
- Penman, D.E., Zachos, J.C., 2018. New constraints on massive carbon release and recovery processes during the Paleocene-Eocene Thermal Maximum. *Environmental Research Letters* 13, 105008.
- Pörtner, H.-O., Karl, D.M., Boyd, P.W., Cheung, W., Lluch-Cota, S.E., Nojiri, Y., Schmidt, D.N., Zavialov, P.O., Alheit, J., Aristegui, J., 2014. Ocean systems, Climate change 2014: impacts, adaptation, and vulnerability. Part A: global and sectoral aspects. contribution of working group II to the fifth assessment report of the intergovernmental panel on climate change. Cambridge University Press, pp. 411-484.
- Punekar, J., Mateo, P., Keller, G., 2014. Effects of Deccan volcanism on paleoenvironment and planktic foraminifera: A global survey. *Geological Society of America Special Papers* 505, 91-116.
- Remmelzwaal, S.R.C., Dixon, S., Parkinson, I.J., Schmidt, D.N., Monteiro, F.M., Sexton, P., Fehr, M.A., Peacock, C., Donnadieu, Y., James, R.H., 2019. Investigating Ocean Deoxygenation During the PETM Through the Cr Isotopic Signature of Foraminifera. *Paleoceanography and Paleoclimatology* 34, 917-929.
- Ridgwell, A., Schmidt, D.N., 2010. Past constraints on the vulnerability of marine calcifiers to massive carbon dioxide release. *Nature Geoscience* 3, 196-200.
- Ruppel, C.D., Kessler, J.D., 2017. The interaction of climate change and methane hydrates. *Reviews of Geophysics* 55, 126-168.
- Rush, W.D., Kiehl, J.T., Shields, C.A., Zachos, J.C., 2021. Increased frequency of extreme precipitation events in the North Atlantic during the PETM: Observations and theory. *Palaeogeography, Palaeoclimatology, Palaeoecology* 568, 110289.
- Saunders, A.D., 2016. Two LIPs and two Earth-system crises: the impact of the North Atlantic Igneous Province and the Siberian Traps on the Earth-surface carbon cycle. *Geological Magazine* 153, 201-222.
- Schaller, M.F., Turrin, B.D., Fung, M.K., Katz, M.E., Swisher, C.C., 2019. Initial ^{40}Ar - ^{39}Ar Ages of the Paleocene-Eocene Boundary Impact Spherules. *Geophysical Research Letters* 46, 9091-9102.
- Scheibner, C., Speijer, R.P., 2008. Late Paleocene–early Eocene Tethyan carbonate platform evolution — A response to long- and short-term paleoclimatic change. *Earth-Science Reviews* 90, 71-102.
- Schulte, P., Scheibner, C., Speijer, R.P., 2011. Fluvial discharge and sea-level changes controlling black shale deposition during the Paleocene–Eocene Thermal Maximum in the Dababiya Quarry section, Egypt. *Chemical Geology* 285, 167-183.
- Scotese, C.R., Wright, N., 2018. PALEOMAP paleodigital elevation models (PaleoDEMS) for the Phanerozoic. PALEOMAP Proj.
- Sheldon, N.D., Smith, S.Y., Stein, R., Ng, M., 2020. Carbon isotope ecology of gymnosperms and implications for paleoclimatic and paleoecological studies. *Global and Planetary Change* 184, 103060.
- Smith, F.A., Wing, S.L., Freeman, K.H., 2007. Magnitude of the carbon isotope excursion at the Paleocene–Eocene thermal maximum: The role of plant community change. *Earth and Planetary Science Letters* 262, 50-65.
- Stassen, P., Thomas, E., Speijer, R.P., 2012. Integrated stratigraphy of the Paleocene-Eocene thermal maximum in the New Jersey Coastal Plain: Toward understanding the effects of global warming in a shelf environment. *Paleoceanography* 27.

- Stokke, E.W., Jones, M.T., Riber, L., Haflidason, H., Midtkandal, I., Schultz, B.P., Svensen, H.H., 2020a. Rapid and sustained environmental responses to global warming: The Paleocene-Eocene Thermal Maximum in the eastern North Sea. *Climate of the Past*.
- Stokke, E.W., Jones, M.T., Riber, L., Haflidason, H., Midtkandal, I., Schultz, B.P., Svensen, H.H., 2021. Rapid and sustained environmental responses to global warming: the Paleocene–Eocene thermal maximum in the eastern North Sea. *Climate of the Past* 17, 1989-2013.
- Stokke, E.W., Jones, M.T., Tierney, J.E., Svensen, H.H., Whiteside, J.H., 2020b. Temperature changes across the Paleocene-Eocene Thermal Maximum—a new high-resolution TEX86 temperature record from the Eastern North Sea Basin. *Earth and Planetary Science Letters* 544, 116388.
- Sulpis, O., Agrawal, P., Wolthers, M., Munhoven, G., Walker, M., Middelburg, J.J., 2022. Aragonite dissolution protects calcite at the seafloor. *Nature Communications* 13, 1104.
- Sun, Y., Zhao, C., Püttmann, W., Kalkreuth, W., Qin, S., 2017. Evidence of widespread wildfires in a coal seam from the middle Permian of the North China Basin. *Lithosphere* 9, 595-608.
- Svensen, H., Planke, S., Corfu, F., 2010. Zircon dating ties NE Atlantic sill emplacement to initial Eocene global warming. *Journal of the Geological Society* 167, 433-436.
- Synnott, D.P., Schwark, L., Dewing, K., Pedersen, P.K., Sanei, H., 2021. Evidence for widespread wildfires and their environmental impact in the Late Cretaceous Canadian Arctic. *Global and Planetary Change* 203, 103515.
- Takeda, K., Kaiho, K., 2007. Faunal turnovers in central Pacific benthic foraminifera during the Paleocene–Eocene thermal maximum. *Palaeogeography, Palaeoclimatology, Palaeoecology* 251, 175-197.
- Tian, S.Y., Yasuhara, M., Huang, H.-H.M., Condamine, F.L., Robinson, M.M., 2021. Shallow marine ecosystem collapse and recovery during the Paleocene-Eocene Thermal Maximum. *Global and Planetary Change* 207, 103649.
- Tipple, B.J., Pagani, M., Krishnan, S., Dirghangi, S.S., Galeotti, S., Agnini, C., Giusberti, L., Rio, D., 2011. Coupled high-resolution marine and terrestrial records of carbon and hydrologic cycles variations during the Paleocene–Eocene Thermal Maximum (PETM). *Earth and Planetary Science Letters* 311, 82-92.
- Tribovillard, N., 2021. Re-assessing copper and nickel enrichments as paleo-productivity proxies. *BSGF-Earth Sciences Bulletin* 192, 54.
- Tribovillard, N., Algeo, T.J., Lyons, T., Riboulleau, A., 2006. Trace metals as paleoredox and paleoproductivity proxies: An update. *Chemical Geology* 232, 12-32.
- Wang, Y., Jiang, S., Cui, Y., Su, H., Jiang, J., Wang, Y., Yang, Z., Hu, X., in revision. Response of calcareous nannoplankton to the Paleocene–Eocene Thermal Maximum in the eastern Tethys Ocean. *Global and Planetary Change*.
- Westerhold, T., Röhl, U., Donner, B., Zachos, J.C., 2018. Global extent of early Eocene hyperthermal events: A new Pacific benthic foraminiferal isotope record from Shatsky Rise (ODP Site 1209). *Paleoceanography and Paleoclimatology* 33, 626-642.
- Westhoff, P., Gowik, U., 2010. Evolution of C4 photosynthesis—looking for the master switch. *Plant Physiology* 154, 598-601.
- Willard, D.A., Donders, T.H., Reichgelt, T., Greenwood, D.R., Sangiorgi, F., Peterse, F., Nierop, K.G.J., Frieling, J., Schouten, S., Sluijs, A., 2019. Arctic vegetation, temperature, and hydrology during Early Eocene transient global warming events. *Global and Planetary Change* 178, 139-152.
- Wing, S.L., Harrington, G.J., Smith, F.A., Bloch, J.I., Boyer, D.M., Freeman, K.H., 2005. Transient floral change and rapid global warming at the Paleocene-Eocene boundary. *Science* 310, 993-996.
- Wu, Y., Hain, M.P., Humphreys, M.P., Hartman, S., Tyrrell, T., 2019. What drives the latitudinal gradient in open-ocean surface dissolved inorganic carbon concentration? *Biogeosciences* 16, 2661-2681.

- Xie, Y., Wu, F., Fang, X., 2022. A transient south subtropical forest ecosystem in central China driven by rapid global warming during the Paleocene-Eocene Thermal Maximum. *Gondwana Research* 101, 192-202.
- Zachos, J.C., Dickens, G.R., Zeebe, R.E., 2008. An early Cenozoic perspective on greenhouse warming and carbon-cycle dynamics. *Nature* 451, 279-283.
- Zachos, J.C., Rohl, U., Schellenberg, S.A., Sluijs, A., Hodell, D.A., Kelly, D.C., Thomas, E., Nicolo, M., Raffi, I., Lourens, L.J., McCarren, H., Kroon, D., 2005. Rapid Acidification of the Ocean During the Paleocene-Eocene Thermal Maximum. *Science* 308, 1611-1615.
- Zachos, J.C., Wara, M.W., Bohaty, S., Delaney, M.L., Petrizzo, M.R., Brill, A., Bralower, T.J., Premoli-Silva, I., 2003. A transient rise in tropical sea surface temperature during the Paleocene-Eocene thermal maximum. *Science* 302, 1551-1554.
- Zeebe, R.E., 2013. What caused the long duration of the Paleocene-Eocene Thermal Maximum? *Paleoceanography* 28, 440-452.
- Zeebe, R.E., Lourens, L.J., 2019. Solar System chaos and the Paleocene–Eocene boundary age constrained by geology and astronomy. *Science* 365, 926-929.
- Zeebe, R.E., Zachos, J.C., Dickens, G.R., 2009. Carbon dioxide forcing alone insufficient to explain Palaeocene–Eocene Thermal Maximum warming. *Nature Geoscience* 2, 576-580.
- Zhang, Q., Wendler, I., Xu, X., Willems, H., Ding, L., 2017. Structure and magnitude of the carbon isotope excursion during the Paleocene-Eocene thermal maximum. *Gondwana Research* 46, 114-123.
- Zhou, X., Thomas, E., Winguth, A.M.E., Ridgwell, A., Scher, H., Hoogakker, B.A.A., Rickaby, R.E.M., Lu, Z., 2016. Expanded oxygen minimum zones during the late Paleocene-early Eocene: Hints from multiproxy comparison and ocean modeling. *Paleoceanography* 31, 1532-1546.
- Zhu, M., Li, M., Wei, S., Song, J., Hu, J., Jia, W., Peng, P.a., 2019. Evaluation of a dichromate oxidation method for the isolation and quantification of black carbon in ancient geological samples. *Organic Geochemistry* 133, 20-31.